Tumour-intrinsic features shape T-cell differentiation through myeloma disease evolution

Kane A. Foster[1], Elise Rees[1], Louise Ainley[1,2], Eileen M. Boyle[1,2], Lydia Lee[1,2], Gwennan Ward[1], Daria Galas-Filipowicz[1], Anna Mikolajczak[1], Emma J. Lyon[1], Dylan Jankovic[1], Jasmine Rahman[1], Mahima Turakhia[1], Imran Uddin[3,4], Gordon Beattie[3,4], Yvette Hoade[1], Catherine Zhu[1,2], James L. Reading[5,6], Ieuan Walker[7,8], Michael Chapman[7,8] Karthik Ramasamy[9], Javier Herrero[10], Benny Chain[11,12], Sergio A. Quezada[6,13], Kwee L. Yong[1,2]

[1]Research Department of Haematology, University College London Cancer Institute, London, United Kingdom.
[2]University College London Hospitals NHS Foundation Trust, London, United Kingdom.
[3]CRUK City of London Centre Single Cell Genomics Facility, UCL Cancer Institute, University College London, London, UK.
[4]Genomics Translational Technology Platform, UCL Cancer Institute, University College London, London, UK.
[5]Pre-Cancer Immunology Laboratory, UCL Cancer Institute, London, UK.
[6]Cancer Research UK Lung Cancer Centre of Excellence, UCL Cancer Institute, London, UK.
[7]MRC Toxicology Unit, Cambridge, United Kingdom.
[8]Cambridge University Hospitals NHS Trust, Cambridge, United Kingdom.
[9]Oxford University Hospitals, NHS Foundation Trust, Oxford, UK.
[10]Bill Lyons Informatics Centre, University College London Cancer Institute, London, United Kingdom.
[11]Division of Infection and Immunity, University College London, London, UK.
[12]Department of Computer Sciences, University College London, London, UK.
[13]Immune Regulation and Tumour Immunotherapy group, Cancer Immunology Unit, Research Department of Haematology, University College London Cancer Institute.

Abstract

The haematological malignancy multiple myeloma is associated with skewed T-cell activation and function. T-cell alterations are detectable in asymptomatic myeloma precursor conditions and have the potential to identify precursor patients at imminent risk of progression. However, what myeloma-associated T-cells alterations represent mechanistically, how they relate to tumour burden and gene expression, and what influences high inter-patient variability in immune composition remains unknown. Here, we assembled the largest ever dataset of published and newly-generated single-cell RNA and TCR sequencing of the marrow and blood from patients with myeloma, precursor conditions, and age-matched non-cancer controls. We show myeloma is not associated with T-cell exhaustion and instead defined by a pattern of T-cell differentiation resembling antigen-driven terminal memory differentiation. Myeloma-associated T-cell differentiation was dependent on tumour-intrinsic features including tumour burden and tumour expression of antigen-presentation genes. Expanded TCR clones accumulating in myeloma were not enriched for viral specificity and were detected in effector states in highly infiltrated marrows. Together, these results suggest anti-tumour immunity drives a novel form of cancer-associated T-cell memory differentiation in myeloma.

44 **Introduction**

45

46 T-cells are polyfunctional immune cells and fundamental players in anti-tumour immunity[1]. In
47 solid cancers, evidence suggests early in carcinogenesis tumour growth can be curtailed by
48 tumour-reactive T-cells[1,2]. However, persistent activation drives these cells away from
49 functional memory states towards a hypo-responsive state of terminal differentiation termed
50 exhaustion[3,4], characterised by the expression of immune checkpoint molecules like
51 programmed cell death protein 1 (PD1)[5], contributing to cancer progression in solid cancers.
52 This complex interaction is believed to shape tumours from the early precursor stages to
53 relapsed and refractory disease[1]. Understanding these insights have refined the treatment of
54 solid tumours through the development of immunotherapies targeting exhausted T-cells[6].

55

56 Multiple myeloma (MM) is a haematological malignancy of bone marrow (BM) plasma cells
57 that is largely incurable[7,8]. Two precursor conditions of increasing severity precede MM:
58 Monoclonal Gammopathy of Undetermined Significance (MGUS) and then Smouldering
59 Multiple Myeloma (SMM). They differ in their risk of progression to overt myeloma with MGUS
60 and SMM being associated with a 5-year progression rate of approximately 7% and 50%
61 respectively[9]. While not every MGUS or SMM patient will progress, virtually every MM patient
62 has transitioned through these stages[10]. Thus, there is a pressing clinical need to identify
63 asymptomatic patients with precursor conditions at imminent risk of progression. Current risk
64 factors rely largely on tumour bulk[11], namely the levels of plasma cell infiltration in the bone
65 marrow and serum concentrations of paraprotein (malignant cell-derived clonal
66 immunoglobulin) and beta-2 microglobulin (B2m)[9]. However, the role of the BM tumour
67 microenvironment, particularly T-cells, in progression remains poorly understood.
68 Understanding how myeloma drives alterations in T cell state and function is complicated by
69 the influence of patient advanced age and marrow homeostatic T-cell differentiation[7,12,13].

This, together with high inter-individual immune heterogeneity, confounds identifying associations between T-cells and tumour biology or progression.

To solve this, we combined over a million single cells from 295 samples from 237 donors using newly-generated single-cell RNA sequencing (scRNA-seq) and T-cell receptor (TCR) sequencing (scTCR-seq) data and 11 published studies[14,15,24,16–23], allowing us to interrogate T-cell dynamics while controlling for natural and tumour-associated sources of inter-individual variation. We show for the first time that the T-cell landscape associated with myeloma possess features of antigen-driven terminal memory differentiation and highlight the features of tumour biology driving this. These results suggest that anti-tumour immunity underpins a novel form of tumour-associated T-cell differentiation in myeloma.

Results

Effective integration of scRNA-seq datasets allows a detailed classification of immune cell populations

To study immune differentiation through myeloma disease evolution we generated a large scRNA-seq map of BM and peripheral blood (PB) cells from untreated MGUS (n = 20, 9%), SMM (n = 58, 25%) and MM (n = 54, 23%) patients alongside non-cancer controls (n = 102, 44%; Fig. 1a, Extended Data Fig. 1a, Supplemental Table 1). Patients were older than controls (controls median 55 range 21–87, MGUS median 62 range: 41–81, SMM median 62 range: 29–81, MM median 62 range: 38–77; Fig. 1b). As expected, plasma cell infiltration of the bone marrow and serum paraprotein levels rose with from SMM to MM (infiltration P = 0.001, paraprotein $P < 0.05$, Wilcoxon test; Fig. 1c).

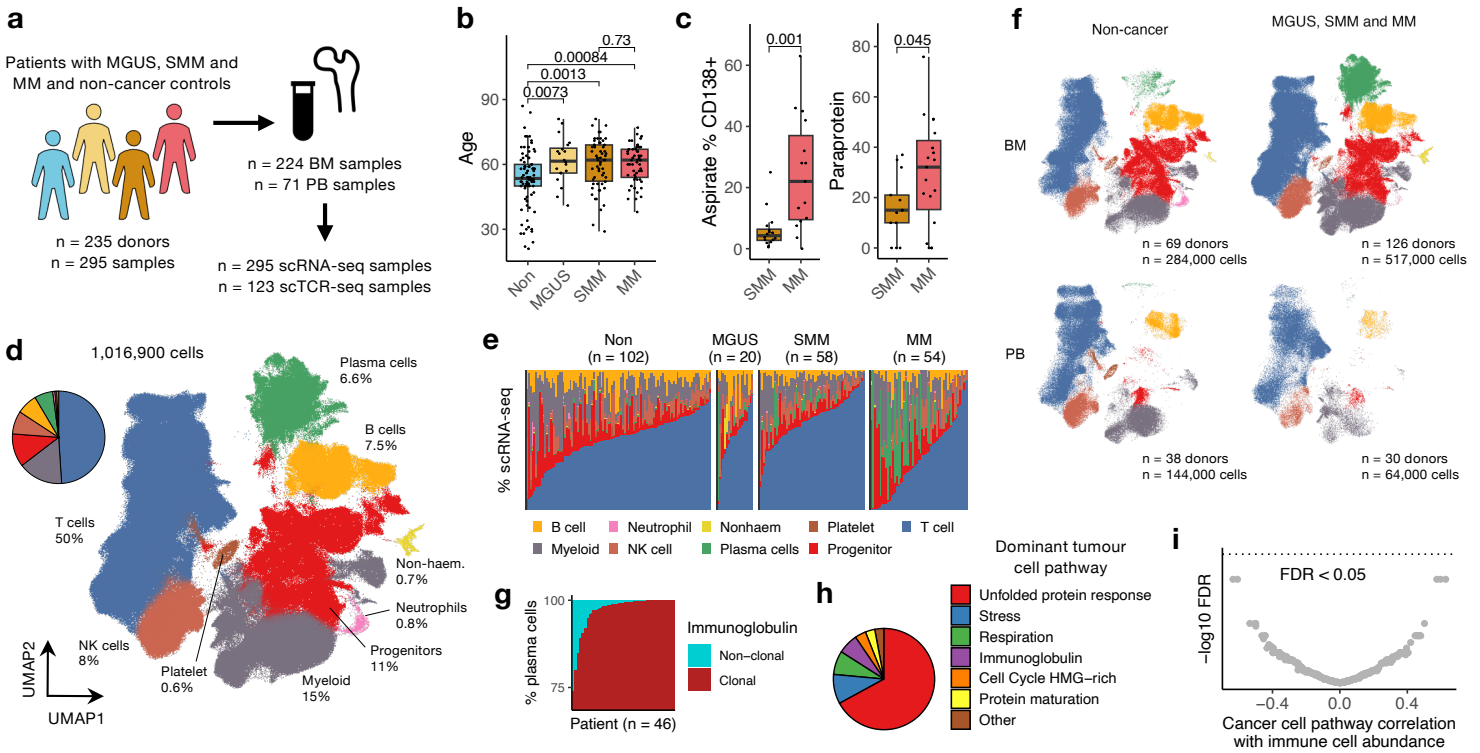

Fig. 1 | Single cell phenotypes are harmonized in a large integrated scRNAseq dataset of patients with myeloma and precursor conditions and non-cancer controls. a, Schematic depicting the cohort, tissue types (BM, bone marrow; PB, peripheral blood), and singe-cell data types included in the study. **b**, Box plot showing the distribution of age (years) in non-cancer controls (n = 86), MGUS (n = 20), SMM (n = 58) and MM (n = 53) patients. **c**, Box plots showing the distribution of aspirate % CD138+ (left) and paraprotein values (right) in SMM (n = 13) and MM (n = 19) patients. **d**, Visualisation of all cells in the dataset by uniform manifold approximation and projection (UMAP). The colour each point (cell) represents the indicated cell type cluster. The percentage of all cells occupied by each cluster is inset. **e**, Bar chart showing the proportion of each cluster for each individual donor (columns) for each cohort. **f**, UMAP as in (**d**) separated by cohort (columns) and tissue type (rows). The number of donors and cells for each separation is inset. **g**. Bar chart showing the proportion of plasma cells with clonal or non-clonal immunoglobulin usage. Plasma cells with clonal immunoglobulin usage were classified as tumour cells. **h**. Pie chart quantify the proportion of each pan-cancer transcriptional pathway which was the most highly expressed (dominant) in tumour cells across all patients. **i**, Dot plot showing FDR-adjusted *P* values and correlation coefficients between cell type cluster abundance (as a proportion of non-plasma cells) and pan-cancer transcriptional pathway expression in tumour cells (n = 45 patients). Box plots represent the first and third quartiles around the median with whiskers extending 1.5 times the interquartile range. *P* values shown on box plots were calculated by two-sided Wilcoxon test.

96 Following quality control and correcting for batch effects (see Methods), Extended Data Fig.
97 1b), cells were clustered to 9 major cell types and phenotyped using RNA expression, protein
98 expression via cellular indexing of transcriptomes and epitopes (CITE-seq), and *de novo* label
99 prediction tools (Fig.1d, Extended Data Fig. 1c,d). T-cells (defined by co-expression of *CD3D,*
100 *CD3E, CD3G*, *CD8A* and *CD4* RNA and CD3 protein) comprised roughly half (50.2%) the cells
101 in the dataset (Fig. 1e), with another quarter occupied by similar proportions of myeloid cells
102 (*FCN1*+*FCER1G*+CD14+; 15%) and haematogenic progenitors (*CD34*+*MPO*+*TYMS*+; 11%).
103 The remainder of the dataset was comprised of equivalent numbers of NK cells
104 (*KLRD1*+*FCG3RA*+CD56+; 8%), B cells (*CD79A*+CD19+; 7.5%), and plasma cells
105 (*MZB1*+*SDC1*+; 6.6%), alongside small (<1% total counts) clusters of neutrophils
106 (*NEAT1*+*NAMPT*+), non-haemopoietic cells (*CXCL12*+*COL3A*+), and platelets (*PPBP*+*PF4*+).
107
108 Despite the heterologous sorting strategies employed by different studies (Extended Data
109 Fig. 1b), we identified major determinants of cellular composition in our dataset (Fig. 1f).
110 Plasma cells and progenitors were enriched in the BM relative to PB ($P < 0.001$ and $P < 0.001$,
111 respectively, Wilcoxon test), suggesting a relative lack of haemodilution in BM aspirates. As
112 expected, plasma cells were most highly enriched in the BM of patients relative to controls
113 ($P < 0.001$, Wilcoxon test). However, the global distribution of cell types was otherwise similar
114 in diseased and controls marrows, suggesting progression to myeloma may be associated
115 with more granular alterations to immune composition.
116
117 Overall, we analysed 1,009,317 cells from 234 individuals with RNA and clinical data, 109
118 with TCR and 1 with CITE-seq data, including 224 BM and 71 PB samples. This resource
119 represents a large cross-sectional analysis of controls and myeloma disease stages and
120 reliably discriminate key immune phenotypes of non-cancer controls and myeloma patients
121 through disease evolution.

122

123 *Recurrent transcriptional pathways in malignant plasma cells underpin progression and*
124 *outcome*

125

126 Next, we sought to characterise more granular features associated with disease evolution
127 that may reveal tumour-immune cross-talk by conducting an analysis of tumour cells.
128 Malignant clones, identified by clonal immunoglobulin usage (see Methods; Extended Data
129 Fig. 2a-c), composed the majority of plasma cells in all patients but were most abundant in
130 MM (Fig. 1g and Extended Data Fig. 2f). To overcome inter-patient tumour transcriptional
131 heterogeneity we scored 67,656 plasma cells from 46 patients with a recently published set
132 of pan-cancer transcriptional pathways[25] (Extended Data Fig.2e, Supplemental Table 2). The
133 pathway most highly expressed by tumour cells corresponded to the unfolded protein
134 response (67% tumour cells, Fig. 1h), with the remaining cells defined by pathways reflecting
135 cellular stress, respiration, or other biological processes.

136

137 To explore the significance of these pathways in disease evolution, we compared their
138 expression in SMM (n = 17) and MM (n = 29; Extended Data Fig. 2f-g), analysed associations
139 with local marrow infiltration (Extended Data Fig. 2h), and overall survival in MM patients from
140 the CoMMpass study[26] (Extended Data Fig. 2i). We identified 18 pathways significantly
141 associated with progression or marrow infiltration, of which 6 were associated with outcome.
142 Broadly, pathways reflecting proteostasis such as the unfolded protein response were
143 characteristic of SMM ($P < 0.001$, Wilcoxon test), whereas more functionally diverse set of
144 pathways were enriched at progression (Extended Data Fig. 2f-g). Proliferation pathways
145 were enriched at progression ($P = 0.07$, Wilcoxon test), in highly infiltrated marrows ($R = 0.42$,
146 $P = 0.03$, Pearson correlation), and associated with significantly shorter overall survival ($P <$
147 0.001, log-rank test; Extended Data Fig. 2i). Conversely, a SMM-enriched pathway

148 characterised by immunoglobulin genes was more frequently highly-expressed in less-
149 infiltrated marrows and association with more favourable outcome ($P < 0.001$, log-rank test).
150 This suggests plasma cells retaining normal functions, such as proteostasis[27], were more
151 common in low risk-and low burden disease, whereas more proliferative states are
152 associated with worse outcome.
153
154 Cellular stress was among the pathways more frequently expressed in MM (P = 0.007,
155 Wilcoxon test; Extended Data Fig. 2e). We extricated this pathway from *in vitro* stressors
156 such as those introduced by sample processing (Extended Data Fig. 2j). Closer inspection of
157 tumour cells highly expressing the stress pathway revealed an enrichment of genes also
158 associated with cell death ($P = 0.02$, GSEA of programmed cell death pathway; Extended
159 Data Fig. 2k). Death pathways were enriched at progression and positively correlated with
160 tumour burden (Extended Data Fig. 2k, Supplemental Table 2), suggesting this stress
161 pathway may reflect death-associated processes. Despite an enrichment at progression,
162 high expression of the stress pathway was associated with superior outcome ($P = 0.014$, log-
163 rank test; Extended Data Fig. 2i), suggesting a more complex relationship for this pathway
164 through disease evolution possibly related to immune correlates.
165
166 Finally, we compared tumour pathways with immune composition. Tumour cell pathway
167 expression was not associated with the abundance (as a fraction of non-plasma cells) of cell
168 types in the BM (all individual cell type–tumour pathway correlations adjusted $P > 0.05$,
169 Pearson correlation; Fig. 1i).
170
171 Together, this data show how the transcriptional activity of tumour cells is influenced related
172 to progression, infiltration, and outcome. However, connecting these pathways to tumour–
173 immune interactions may require a more granular overview of immune cells.

174

175 *In-depth T-cell phenotyping reveals myeloma is not enriched in exhausted cells and T-cell*
176 *composition is similar in health and disease*

177

178 To more deeply probe immune perturbations and tumour-immune cross-talk in disease
179 evolution, T-cells were isolated, re-integrated and re-clustered to 19 discrete phenotypes and
180 transcriptional states based on expression of canonical RNA and protein markers (Fig. 2a-b,
181 Extended Data Fig.3a-c, Supplemental Tables 2-3)[4,28–30]. CD4+ cells were predominantly
182 naïve (Tn, 49% of CD4+T-cells) and central memory (Tcm, 21%) cells, and the remainder in
183 regulatory (Treg, 8.4%), helper (Th17 7.2%; T effector memory, Tem 6.1%) or cytotoxic
184 (cytotoxic T lymphocyte, CTL, 8.7%) states. CD8+ cells were classified into a more linear
185 trajectory spanning earlier Tn (20% of CD8+T-cells), Tcm (4.6%) and *IL7R*-expressing
186 effector memory (Tem.IL7R, 12%) through *PDCD1*+ activated Tem (TemActive, 22%) to more
187 later differentiated *GZMB*+ terminal Tem (TemTerm, 18%) and Tem re-expressing CD45RA
188 (TEMRA, 15.1%) subsets, alongside tissue resident (Trm, 5.1%) and exhausted (Tex, 0.7%)
189 clusters. Invariant subsets, comprising γδ T-cells (gdT) and mucosal-associated invariant T-
190 cells (MAIT), proliferating and interferon-induced clusters were also identified. This included
191 an interferon-induced cluster resembling effector T-cells characterised by expression of IFN-
192 induced protein with tetratricopeptide repeats 2 (*IFIT2*) alongside effector molecules *TNF* and
193 *IFNG* (Teff.IFIT2). This functional annotation was consistent with patterns of TCR expansion
194 (Fig. 2c, Extended Data Fig. 3d-e), with the most clonally expanded clusters expressing the
195 highest level of late differentiation markers. Our phenotypes showed high concordance with
196 published and predicted cluster labels (Extended Data Fig. 3f), arguing for a faithful
197 representation of T-cell phenotypes in our integrated dataset.

198

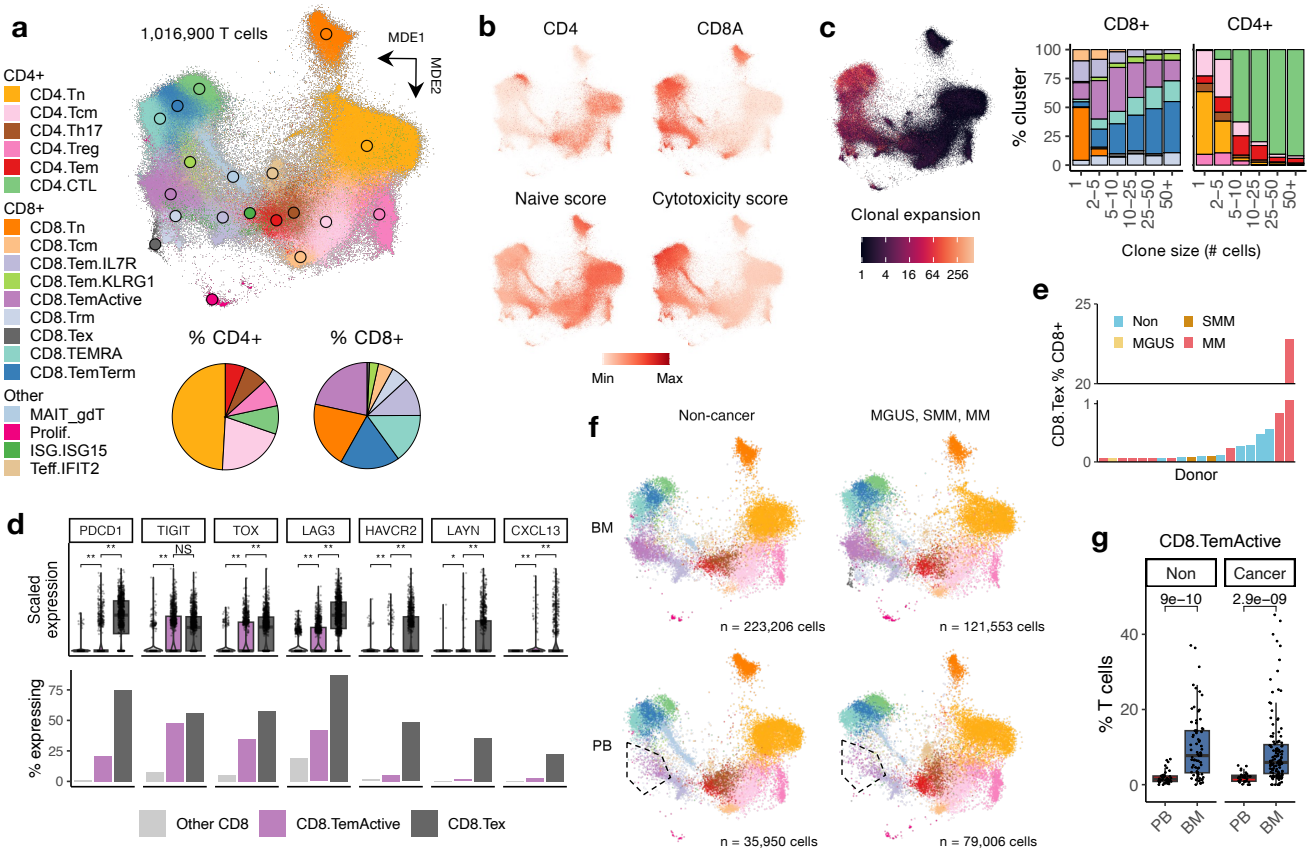

Fig. 2 | The T cell landscape of myeloma is not enriched in exhausted cells and reflects intrinsic marrow biology. a, Visualisation of all T cells in the dataset by minimum-distortion embedding (MDE). The colour each point (cell) represents the T cell cluster indicated by the legend. Pie charts depict the percentage of CD4+ (left) and CD8+ (right) T cell clusters in the dataset. **b**, MDE plots showing the expression of *CD4*, *CD8A*, and naïve and cytotoxic genes signatures. **c**, Left, MDE plot showing the clonal expansion of T cell receptor (TCR) clones (calculated as the number of times a unique clone was seen). Right, Bar chart showing the proportion of each CD8+ (left) and CD4+ (right) cluster among TCR clones of the indicated size. Bar colour represents T cell cluster indicated in (**a**). **d**, Box plots showing the expression (top) and bar plots showing the percentage of cells expressing (bottom, fraction of cells with non-zero expression) indicated T cell exhaustion associated genes in CD8.Tex, CD8.TemActive and other CD8+ T cell clusters. For the three groups a random sample of 1,000 cells from Zheng et al. are shown. *P* values calculated by Wilcoxon test, ** = $P < 0.001$, * = $P < 0.01$, NS = $P > 0.05$. **e**, Bar plot showing the abundance of CD8.Tex as a percentage of total CD8+ T cells for the twenty donors with the highest abundance of CD8.Tex. **f**, MDE as in (**a**) separated by cohort (columns) and tissue (rows: bone marrow, BM; peripheral blood, PB). For the four groups a random sample of 20,000 cells is shown. The total number of cells for each separation is inset. The CD8.TemActive cluster is circled. **g**, Box plot showing the abundance of CD8.TemActive as a percentage of T cells in the PB and BM of non-cancer controls (Non, PB n = 39, BM n = 73; left) and SMM and MM patients (Cancer, PB n = 30, BM n = 123; right). Box plots represent the first and third quartiles around the median with whiskers extending 1.5 times the interquartile range. *P* values shown on box plots were calculated by two-sided Wilcoxon test.

199 We validated our proposed BM T-cell landscape by employing CyTOF on an independent
200 cohort of 9 SMM and 11 MM donors, assaying 940,000 cells with 46 markers (Supplemental
201 Table 4). *De novo* clustering and a comparison of T-cell clusters across technologies (see
202 Methods) revealed a range of phenotypes closely matched and enhanced those seen in our
203 scRNA-seq dataset (Extended Data Fig. 4). For example, expression of the CD57
204 glycoepitope on GZMB+ CD28– CD8+Tem (CD8.Tem-Term) suggested a phenotype of
205 terminal effector memory cells[31,32].
206
207 We identified exhausted CD8.Tex by the expression of high levels of *PDCD1* and *TIGIT*,
208 alongside other RNA markers of exhaustion like *CXCL13* and *LAYN*[29]. Importantly, we
209 distinguish CD8.Tex from *GZMK*-expressing CD8.TemActive. CD8.TemActive expressed
210 higher *PDCD1* and *TOX* than non-exhausted bone marrow T-cells ($P < 0.001$ and $P < 0.001$,
211 Wilcoxon test) but less than CD8.Tex ($P < 0.001$ and $P < 0.001$, Wilcoxon test) and lacked
212 other markers of exhaustion like *LAYN* ($P < 0.001$, Wilcoxon test; Fig. 2d, Extended Data Fig.
213 3b) and expressed early differentiation markers like *CD28*. In our CyTOF dataset, expression
214 of PD1 and the exhausted-associated transcription factor TOX[33] were similarly restricted to
215 early CD8+Tem (CD45RO+KLRG1+CD28+; Extended Data Fig. 4c). Interestingly, the
216 CD8.Tex cluster was almost entirely composed of cells from a single myeloma patient (1181
217 of 1222 cells, 97%; Fig. 2e) who contributed the majority of exhaustion marker-expressing
218 cells (Extended Data Fig. 2g), suggesting CD8.Tex were a donor-specific phenomenon.
219 Similar observations were made for the CD8.Trm cluster, being mostly composed of 2
220 samples from the same study as the donors-specific CD8.Tex (27.4% and 26.1% of cells;
221 Extended Data Fig. 5a). These data lead us to suggest that exhausted T-cells are rarely seen
222 in myeloma and the more frequent PD1-expressing activated CD8+Tem are distinct from
223 exhausted cells.
224

225 Similar T-cell phenotypes were observed in the BM and PB (Fig. 2f), but the proportion of T-
226 cell clusters differed between tissues (Extended Data Fig. 3h). Notably, CD8.TemActive were
227 enriched in the BM of both patients and controls ($P < 0.001$ and $P < 0.001$, Fig. 2g),
228 suggesting intrinsic marrow biology regulates the abundance of this subsets in health and
229 myeloma.
230
231 *T-cell differentiation skewing occurs in disease independent of age and presents similarly in*
232 *pre-malignant SMM and overt MM*
233
234 We next asked how the relative abundance of T-cell subsets in the BM was altered across
235 disease stages. BM T-cell composition was strikingly similar in patients and controls (Fig. 3a,
236 Extended Data Fig. 5a), with the exception of donor-specific CD8.Tex clusters. We next
237 compared the T-cell composition of controls with each myeloma disease stage in turn,
238 statistically controlling for age. The most prominent difference in BM T-cell composition
239 between health and disease was the loss of naïve, CD4.Th17 and MAIT cells and an
240 enrichment of *GZMB*-expressing memory T-cell clusters (FDR-adjusted $P < 0.1$ for all, linear
241 models; Fig. 3b, Extended Data Fig. 5b). When removing the one patient who contributed the
242 majority of CD8.Tex cells (97% cells; Fig. 2e), this cluster was not enriched in MM relative to
243 controls ($P = 0.54$, linear models). As non-cancer controls included hip replacement and
244 deceased donors, we repeated our analysis with only healthy donors and obtained the same
245 results (Extended Data Fig. 5c). Low-risk MGUS possessed a T-cell composition with the
246 fewest differences to control marrows. Conversely, T-cell composition was similar between
247 the higher-risk but pre-cancerous SMM and symptomatic MM (Extended Data Fig. 5d). While
248 the normalised abundance of CD8.Tex was lower in SMM than MM independent of age ($P <$
249 0.001, linear model), in terms of unnormalized counts this only represented 8 MM patients
250 with a median of 1 CD8.Tex cells each suggesting this did not represent a meaningful

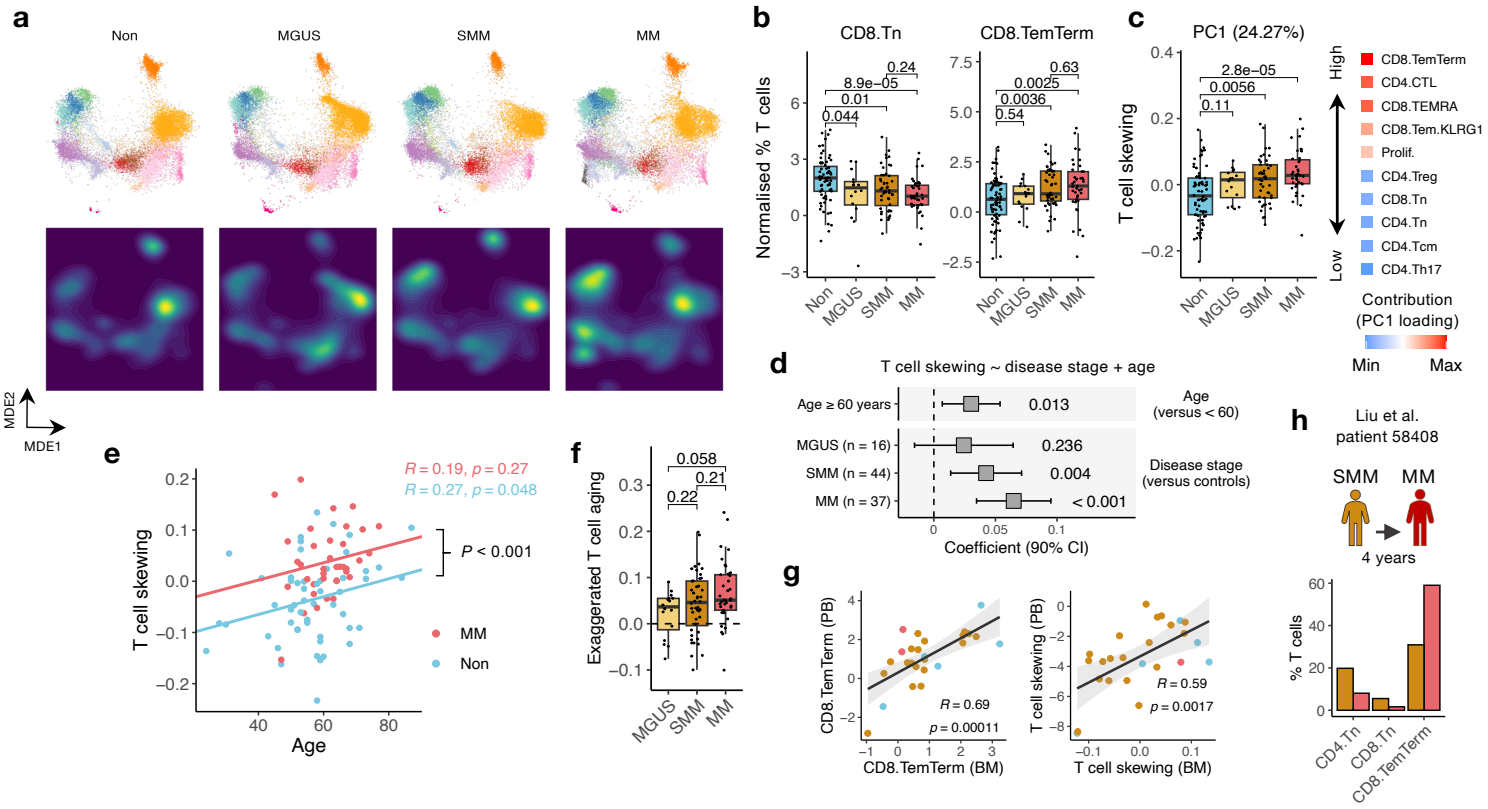

Fig.3 | Step-wise alterations to bone marrow T cell composition occur through myeloma disease evolution. **a**, Visualisation of BM T cells clusters (top) and cell density (bottom) by minimum-distortion embedding (MDE) in non-cancer controls (Non), MGUS, SMM and MM patients. For the four groups a random sample of 20,000 cells is shown. **b**, Box plots showing the normalised abundance (see Methods) of CD8.Tn (left) and CD8.TemTerm (right) in the BM as a percentage of T cells in non-cancer controls (n = 71), MGUS (n = 16), SMM (n = 48) and MM (n = 41) patients. **c**, Left, Box plot showing the value of the T cell skewing (the first principal component (PC1), 24.27% variance, calculated on BM samples only) in Non (n = 68), MGUS (n = 16), SMM (n = 45) and MM (n = 39) patients. Right, representation of the clusters with the highest and lowest contribution (loading) to PC1. For example, a high PC1 value corresponds to a high number of CD8.TemTerm. **d**, Forest plot showing the relationship between T cell skewing and disease stage (MGUS (n = 16), SMM (n = 44) and MM (n = 37) relative to controls (n = 53)) and age (binarized to ≥ median age (60 years)). Coefficients with 90% confident interval (CI) and *P* values from linear model (see Methods) are inset. **e**, Dot plot showing the correlation between T cell skewing and age in non-cancer controls and MM patients. *P* value from linear model is inset. **f**, Box plot showing exaggerated T cell aging (the residuals between a patient's PC1 values and a model of PC1 and age in controls only, see Methods) in MGUS, SMM and MM patients. Residuals of zero (T cell skewing expected for patient's age) is indicated with dashed line. **g**, Dot plots showing the correlation between the abundance of CD8.TemTerm (left) and T cell skewing (right) in the PB and BM for patients with samples from both tissues. **h**, Upper, Schematic depicting longitudinal sampling of patient 58408 from Liu et al. Lower, Bar plot showing the abundance of indicated T cell cluster in SMM and MM for patient 58408. Box plots represent the first and third quartiles around the median with whiskers extending 1.5 times the interquartile range. *P* values shown on box plots were calculated by two-sided Wilcoxon test. R and *P* values for correlations were calculated by Pearson correlation. Correlation shaded regions represent the 95% confidence interval of linear regression slopes.

enrichment. For patients with available risk data, we saw no significant differences in T-cell composition between international staging system (ISS) and SMM Mayo risk groups[9,34] (Extended Data Fig. 5e). In our smaller CyTOF cohort we noted a trend for the enrichment of CD57+ CD8.Tem-Term in MM relative to SMM (Extended Data Fig. 5f). These results suggest that smouldering and overt myeloma are associated with similar T-cell alterations independent of age.

To interrogate changes to BM T-cells in a less supervised manner we ran principal component analysis (PCA) on patient's T-cell composition. The first principal component explaining the highest fraction of variance in T-cell composition (PC1, 24.27%; Extended Data Fig. 5g) described a compositional shift across clusters from more naïve and early subsets to terminal memory clusters (Fig. 3c). As this composition alteration represented a shift from phenotypes at either end of the T-cell differentiation spectrum[4], we termed PC1 "T-cell skewing". T-cell skewing was highest (indicating an enrichment of terminal memory clusters) in SMM and MM relative to controls independent of age ($P < 0.004$ and $P < 0.001$, respectively, linear model; Fig. 3c-d), demonstrating this metric captured the major alterations to T-cells in myeloma. We noted T-cell skewing was associated with age independent of patient group ($P = 0.013$, linear model, R = 0.28, Pearson correlation; Fig. 3d, Extended Data Fig. 5h) and correlated with age in controls ($P < 0.05$, R = 0.25; Fig. 3e). As T-cell skewing was independently associated with both myeloma and age (Fig. 3d), this component of myeloma-associated T-cell differentiation resembled T-cell alterations seen during aging. Therefore, patients possessed an exaggerated form of the T-cell compositional skewing seen with aging. The degree of exaggerated T-cell aging (see Methods) trended to rise with disease severity (MGUS versus MM, $P = 0.06$, Wilcoxon test; Fig. 3f) and the highest fraction of patients with exaggerated skewing was seen in myeloma (86%) versus MGUS (68%) and SMM (72%).

277

278 PC1 values and the abundance of terminal memory subsets in the BM strongly correlated in
279 the PB of the same patients (Fig. 3g), further indicating a similarity of these changes to
280 systemic T-cell alterations seen with aging[12].

281

282 Finally, in a single patient sampled longitudinally at SMM and at progression to MM we
283 observed the same compositional alternations seen cross-sectionally (Fig. 3h), suggesting
284 these differentiated T-cell phenotypes accumulate longitudinal within patients through
285 disease evolution.

286

287 *Features of antigen-specific responses underpin myeloma-associated T-cell differentiation*

288

289 Next, we analysed features of the TCR repertoire. Repertoire clonality was associated with
290 T-cell skewing in patients independent of age ($P < 0.001$, linear model, R = 0.71; Fig. 4a). We
291 observed similar results when restricting analysis to CD8-expressing memory clones ($P <$
292 0.01, linear model, R = 0.55; Fig. 4a, Extended Data Fig. 6a), with both the clonality and the
293 abundance of expanded clones of this subset was trending for enrichment in MM relative to
294 controls (Fig. 4b). T-cell skewing and CD8+ memory diversity did not correlate in controls (P
295 $= 0.66$, linear model; Extended Data Fig. 6b), suggesting enhanced clonal expansion may be
296 a unique feature T-cell differentiation in myeloma.

297

298 The accumulation of TCRs possessing similar CDR3 sequences can indicate responses
299 against shared antigens[35]. Using tcrdist3[36] we grouped all expanded TCRs in the dataset
300 (11,545 clones) into 279 clusters (composed of 1,014 clones, 8.8% of input; Extended Data
301 Fig. 6c-d, Fig. 4c). This analysis revealed an increasingly large fraction of the TCR repertoire
302 was occupied by clustered clones in MM (median 8.7% range 3-35) relative to SMM (median

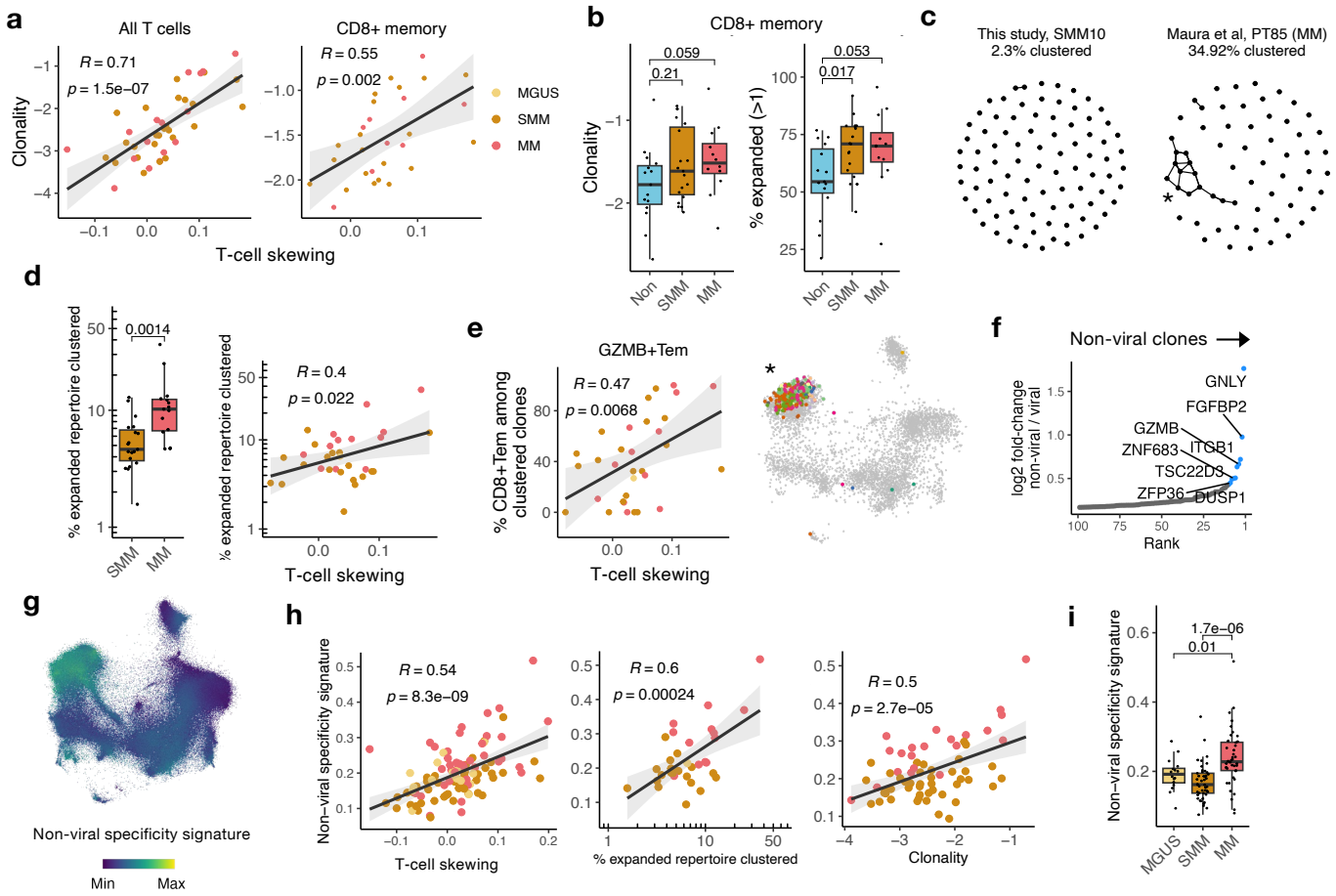

Fig.4 | Features of antigen-experienced T cell receptor repertoires underpin myeloma-associated T cell differentiation. **a**, Dot plots showing the correlation between T cell skewing (PC1 values) and TCR clonality ($\log_{10}$ 1/Simpson's diversity) among all T cell clones (left) and CD8+ memory clones (CD8+ clones, CD8+ clusters excluding CD8.Tn and CD8.Tcm) in MGUS, SMM and MM patients (all T cell clones n = 42, CD8+ memory clones n = 29). **b**, Box plots showing the clonality (left) and abundance of expanded clones (right) of CD8+ memory clones in non-cancer controls (n = 15), SMM (n = 19) and MM (n = 12). **c**, Network plots showing the extent of clustering among expanded (>1) TCRs from two representative patients with low (left) and high (right) percentages of total repertoire clustering. Each node represents a TCR clone and each edge that two TCR clones had a co-clustered alpha or beta sequence. An asterisk indicates a cluster analysed in **e**. **d**, Left, Box plot showing the percentage of clustered expanded TCRs in SMM (n = 19) and MM (n = 15). Right, dot plot showing the correlation between PC1 values and the the percentage of clustered expanded TCRs in MGUS, SMM and MM patients (n = 35). **e**, Left, Dot plot showing the correlation of T cell skewing and the percentage of CD8+Tem (CD8.TemTerm, CD8,TEMRA) among cells from clustered TCR clones. **f**, Results from a differential expression analysis of T cells possessing TCR clones annotated as viral-reactive (see Methods) versus all other clones. Expression testing was performed in 19 patients with a median of 20 viral-reactive and 966 unannotated clones per-patient. The 10 most highly non-viral enriched genes were used to define a non-viral specificity signature and are labelled. **g**, Visualisation of 1,016,900 T cells by minimum-distortion embedding (MDE). The colour each point (cell) represents the non-viral specificity signature score expressed by that T cell. **h**, Dot plots showing the correlation between the mean non-viral specificity signature score per-patient and T cell skewing, the percentage of clustered TCRs among expanded TCRs, and TCR clonality in MGUS, SMM and MM patients. **i**, Box plot showing the mean non-viral specificity signature score in MGUS (n = 16), SMM (n = 45) and MM (n = 40) patients. Box plots represent the first and third quartiles around the median with whiskers extending 1.5 times the interquartile range. *P* values shown on box plots were calculated by two-sided Wilcoxon test. R and *P* values for correlations were calculated by Pearson correlation. Correlation shaded regions represent the 95% confidence interval of linear regression slopes.

303 3.1% range 0-11.3) and this fraction correlated with T-cell skewing (R = 0.4, *P* = 0.02, Pearson
304 correlation; Fig. 4d). T-cell skewing was specifically associated with the clustering of *GZMB*-
305 expressing CD8+ memory cells (R = 0.47, *P* = < 0.01; Fig. 4e), suggesting conserved antigen-
306 specific responses drive T-cell differentiation in myeloma, specifically among *GZMB*-
307 expressing subsets.
308
309 We next explored the T-cell antigen specificity. TCR specificity databases are mostly
310 composed of viral antigens[37–39], allowing us to ask if viral antigen specificities were involved
311 in T-cell differentiation and clonality in myeloma (see Methods). In 19 patients we identified
312 putative HLA-matched specificities for a median of 7 (range 2-88) paired clone per-patient
313 against viral antigens (Extended Data Fig. 6e). Comparing gene expression between clones
314 with and without putative viral-specificity annotations, we observed clones predicted to be
315 non-viral specific expressed genes characteristic of terminal memory such as *GZMB*,
316 perforin/*PRF1* and Hobit/*ZNF683* (Fig. 4f, Supplemental Table 5). We summarised the
317 expression of these genes into a non-viral specificity gene signature (Extended Data Fig. 6f).
318 Non-viral specificity mapped to *GZMB*+ terminal memory clusters (Fig. 4g, Extended Data
319 Fig. 6g), correlated with T-cell skewing, clonality and repertoire clustering (Fig. 4h), and was
320 enriched in MM relative to precursor conditions (Fig. 4i). Together, these data show myeloma-
321 associated T-cell differentiation occurs alongside alterations to the TCR repertoire
322 resembling antigen-direct T-cell immunity which may not reflect the activity of viral-specific
323 TCR clones.
324
325 *Tumour-intrinsic features drive two clonally-related patterns of T-cell differentiation*
326
327 We next asked if features of tumour biology may drive T-cell skewing. We examined serum
328 paraprotein and B2m concentrations, plasma cell marrow infiltration, and tumour cell

329 transcriptional state (Extended Data Fig. 2). As T-cell skewing overlapped in precursor
330 patients and overt MM (Fig. 3c), we looked for associations among all patients independent
331 of disease stage.
332
333 We did not find an association between T-cell skewing and tumour transcriptional state,
334 marrow infiltration, or B2m levels (Fig. 5a, Extended Data Fig. 7a-b). However, we observed
335 a positive correlation between high T-cell skewing and an enrichment of terminal memory
336 cells with paraprotein levels (R = 0.45, P = 0.02, Pearson correlation; Fig. 5a-b, Extend Data
337 Fig. 7c). This association was seen across different disease stage and centres (Extended
338 Data Fig. 7d) and was recapitulated in our CyTOF cohort (Extended Data Fig. 7e). The same
339 paraprotein correlation was also seen with TCR repertoire clonality (R = 0.53, P < 0.001,
340 Pearson correlation; Fig. 5a, Extended Data. 7f). We found the degree of exaggerated T-cell
341 aging was significantly higher in SMM and MM patients with high paraprotein levels
342 independent of disease stage (P = 0.01, linear model; Extended Data Fig. 7g), suggesting
343 paraprotein was the main driver of T-cell skewing in patients.
344
345 We speculated tumour-intrinsic features were associated with individual T-cells clusters
346 independent of overall T-cell skewing. Analysis of T-cell cluster abundance with marrow
347 infiltration and transcriptional pathway scores in tumour cells revealed effector-like Teff.IFIT2
348 cells were enriched in highly-infiltrated marrows populated by stressed tumour cells (marrow
349 infiltration: R = 0.55, tumour stress: R = 0.6; Fig. 5a-b, Extended Data Fig. 7h-i). Several other
350 clusters possessed a significant correlation with tumour stress, including positive and
351 negative associations with CD8.Trm and CD4.Tem, respectively (Extended Data Fig. 7i).
352 Teff.IFIT2 cells were not uniquely defined by stress-associated genes (P = 0.12, GSEA of
353 stress pathway among Teff.IFIT2 marker genes), arguing against this association
354 representing exposure to similar stressors across T and tumour cells. Additionally, the

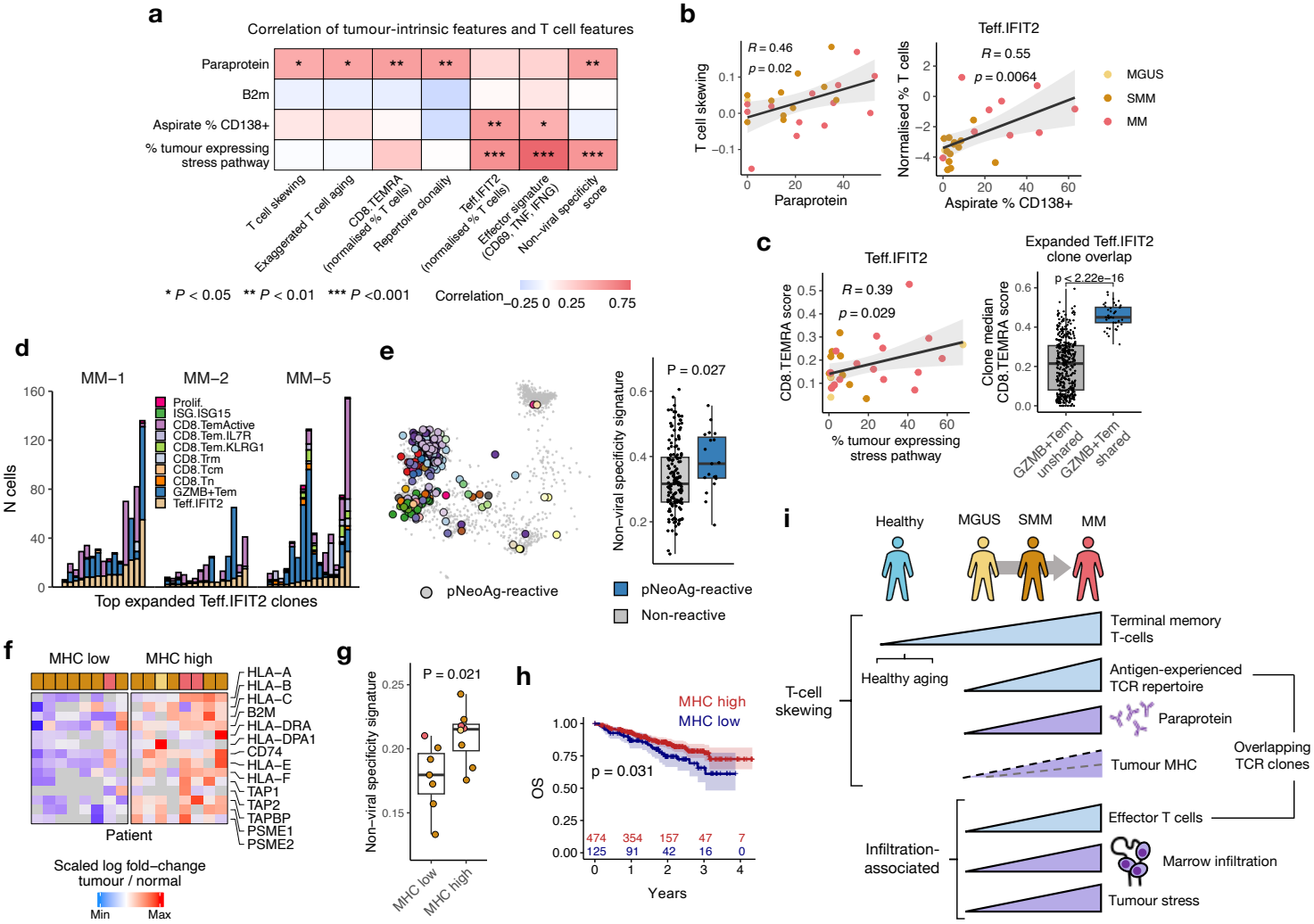

Fig. 5 | Tumour-intrinsic drivers of T cell differentiation indicate anti-tumour immunity contributes to myeloma-associated T cell differentiation. **a**, Heatmap showing the correlation between tumour-intrinsic features (rows) and T cell features (columns) in all patients. Cell colour represents strength of association (correlation) and asterisk degree of significance (Pearson correlation). **b**, Dot plot showing the correlation between T cell skewing (PC1) and paraprotein values (left) and the normalised abundance (see Methods) of Teff.IFIT2 and the aspirate % CD138+ (right). **c**, Left, correlation between the average expression the twenty most significant CD8.TEMRA marker genes among Teff.IFIT2 cells and the the abundance of cancer cells highly expressing stress pathway genes. Right, Box plot showing the median expression of the CD8.TEMRA marker gene score per-clone among cells in the Teff.IFIT2 cluster. Each clone was grouped based on the T cell cluster composition of the remaining cells that composed that clone, specifically the abundance of *GZMB*-expressing Tem clusters (CD8.TEMRA, CD8.TemTerm and CD4.CTL), classifying those which were >50% composed of *GZMB*-expressing clusters as Shared and that those which were not as Unshared. **d**, Bar plot showing the T cell cluster composition of the largest CD8+ clones expanded in the Teff.IFIT2 cluster in three representative myeloma patients. Expanded Teff.IFIT2 clones are predominantly in GZMB+Tem (CD8.TEMRA, CD8.TemTerm and CD4.CTL) clusters. **e**, Left, Visualisation of T cells by minimum-distortion embedding (MDE). The coloured points (cell) represents cells derived from TCR clones predicted as reactive against cancer cell-expressing neoantigens (pNeoAg-reactive, see Methods). Point colour reflects individual clones. Right, Box plot showing the median expression of the non-viral specificity signature in expanded clones annotated as either pNeoAg-reactive or with no annotation. **f**, Heatmap showing the expression of genes significantly up- and down-regulated on cancer cells relative to non-cancer plasma cells across patients. Patients were classified as "MHC high" if their tumour cells had significantly upregulated the antigen processing and presentation pathway relative to non-tumour cells and as "MHC low" if not. **g**, Box plot showing the expression of the non-viral specificity signature in patients with high and low expression of MHC genes (**f**). **h**, Kaplan–Meier curve showing the impact of high (red) and low (blue) scoring of the MHC pathway (**f**) on overall survival in 598 newly-diagnosed untreated multiple myeloma patients enrolled in the ComMMpass trial. *P* value calculated using log-rank test. **i**, schematic representing a summary of findings. Box plots represent the first and third quartiles around the median with whiskers extending 1.5 times the interquartile range. *P* values shown on box plots were calculated by two-sided Wilcoxon test. R and *P* values for correlations were calculated by Pearson correlation. Correlation shaded regions represent the 95% confidence interval of linear regression slopes.

355 expression of a smaller set of T-cell effector genes (*CD69*, *TNF*, *IFNG*) followed the same
356 correlations (marrow infiltration: R = 0.43, tumour stress: R = 0.79, Pearson correlation;
357 Fig.5a, Extended Data Fig. 7j), suggesting a T-cell effector program specifically was
358 associated with infiltration and tumour stress.
359
360 Concurrent tumour-associated T-cell memory and effector differentiation suggests a
361 differentiation process between these two states. Clonally expanded Teff.IFIT2 cells enriched
362 in highly-infiltrated marrows populated by stressed tumours expressed markers
363 characteristic of *GZMB*-expressing CD8.TEMRA (Fig. 5c, Extended Data Fig. 7k). This
364 expression was attributable to cells derived from *GZMB*-expressing CD8+ terminal memory
365 clones (Fig. 5c) and clonally expanded Teff.IFIT2 clones predominantly in these *GZMB*+
366 phenotypes (Fig. 5d, Extended Data Fig. 7k). Therefore, terminally differentiated memory
367 clones accumulating in myeloma are continuous with effector-like T-cells in infiltrated
368 marrows, suggesting these states are linked by a T-cell differentiation pathway.
369
370 *Myeloma-associated T-cell differentiation possesses features of anti-tumour immunity*
371
372 The enrichment of clonal memory T-cells independent of age and viral specificity in myeloma
373 suggests tumour-directed T-cell responses. To investigate this, we identified TCR predicted
374 to bind autologous tumour neoantigens in two patients (see Methods). Expanded TCRs
375 predicted to bind neoantigens mapped to terminal memory and effector-like cells
376 (CD8.TemTerm: odds ratio = 3.2, $P < 0.001$, ISG.IFIT2: odds ratio = 2.5, $P < 0.001$, Fischer's
377 exact test; Fig. 5h, Extended Data Fig. 8a) and possessed significantly higher expression of
378 the non-viral specificity signature (P = 0.027, Wilcoxon test) , suggesting tumour antigen-
379 specific may be involved in MM-associated T-cell differentiation.
380

381 Tumour antigen-driven T-cell differentiation suggests a degree of tumour immunogenicity.
382 Therefore, we examined the expression of antigen-expression genes in tumour cells. T-cell
383 skewing and non-viral specificity signature expression did not correlate with tumour MHC-
384 associated pathways (Extended Data Fig. 7a, 8b), possibly as these pathways reflect MHC
385 in the context of interferon signalling[25]. We identified *de novo* pathways enriched among each
386 individual patient's tumour cells (see Methods), revealing MHC and antigen processing and
387 presentation genes were frequently upregulated by individual tumours (*Antigen processing*
388 *and presentation* pathway, GSEA adjusted $P < 0.1$ in 6 of 16 (37.5%) of tumours tested; Fig.
389 5f, Extended Data Fig. 8c, Supplemental Table 2). Non-viral specificity signature expression
390 was highest in patient's whose tumour cells significantly upregulated MHC pathways (P =
391 0.021, Wilcoxon test; Fig. 5g), suggesting the reactivity component of MM-association T-cell
392 differentiation was connected to tumour MHC class I expression and potentially antigen
393 presentation. Finally, in CoMMpass, patients whose tumours highly expressed MHC pathway
394 genes had superior outcome (P = 0.031, log-rank test; Fig. 5h), suggesting that T-cell
395 differentiation dynamics associated with high tumour MHC class I expression may influence
396 clinical outcomes.
397

398 **Discussion**

399 Recent insights into anti-tumour T-cell immunity have largely derived from studies of solid
400 tumours but a similar understanding in haematological malignancies is lacking. Myeloma has
401 a clinically-defined precursor disease phase lends itself to the study of how T-cell
402 differentiation is altered with disease evolution.
403

404 In this study, we curated a large cohort of single-cell data across 11 studies and 234 donors
405 to identify myeloma-specific alterations to T-cells, which we enhanced through the analysis

406 of the TCR repertoire, the BM and PB, and tumour cell transcriptional state. This allowed us
407 to identify the specific features of tumour biology associated with T-cell differentiation in
408 myeloma, independent of natural heterogeneity attributable to tissue localisation and age.
409 We describe two patterns of myeloma-associated T-cell differentiation (Fig. 5i): (1) terminal
410 memory T-cells with features of antigen-specific differentiation and lacking viral-specificity
411 accumulate dependent on serum paraprotein and tumour MHC expression; and (2) effector
412 T-cells are enriched in highly-infiltrated marrows populated by stressed tumour cells. As
413 these two myeloma-associated T-cell subsets are clonally related (Fig. 5c-d), we suggest
414 they represent the differentiation of tumour-reactive clones accumulating alongside anti-
415 tumour immunity through disease evolution (Extended Data Fig. 9).
416
417 It will be important to see if other immune subsets possess similar associations. In pursuit of
418 this goal, we make our integrated data available for other researchers.
419
420 Our results resolve conflicting reports on the presence of exhausted T-cells in myeloma and
421 a poor history of checkpoint inhibition in this setting[24,40,41]. We show exhausted T-cells are
422 not pervasively enriched in myeloma and are distinct from the more abundant activated
423 CD8+Tem cells which match previous descriptions of PD1-expressing CD8+ T-cells in
424 healthy donors[42,43]. The presence of these “pseudo-exhausted” cells may have led to
425 misidentification of exhausted cells in myeloma patients[40,44], especially given their enrichment
426 in the bone marrow (Fig. 2g). Additionally, we did not connect an exhaustion phenotype to
427 tumour-specificity (Fig. 4f, 5e), suggesting exhaustion-associated loss of tumour-reactive T-
428 cells may not drive progression as is thought in solid tumours[1]. However, activated CD8+Tem
429 may still be involved in bone marrow pathology, with cells resembling this phenotype
430 possessing negative and positive associations with the response to T-cell engager (TCE)
431 therapy in advanced MM and combination therapy in SMM, respectively[23,45].

432

433 We show myeloma is associated with an enrichment of terminally differentiated clonal
434 memory T-cells. This analysis extends previous reports[14,21,46] by demonstrating an
435 independence from age and showing concurrent changes to the TCR repertoire and systemic
436 T-cell compartment. These alterations are similar to T-cell immunosenescence changes seen
437 during aging[12], meaning SMM and MM patients have prematurely aged T-cell compartments
438 (Fig. 3d). Exaggerated T cell aging in precursor conditions may explain the increased risk of
439 infections in these patients[47], and impede the ability to control tumour growth, facilitating
440 progression. Prior immunosenescence may also predispose individuals to cancer
441 development hence present more frequently in patients[48]. Additionally, this pattern of T-cell
442 differentiation could mechanistically represent anti-tumour T-cell responses. Patient-derived
443 T-cells show evidence of tumour-reactivity in myeloma[49,50], specifically terminal memory
444 CD8+ phenotypes[51]. This supports our *in silico* evidence that tumour-reactivity may
445 contribute to myeloma-associated T-cell differentiation (Fig. 4g,h, 5e). This suggests that
446 effector T-cells enriched in infiltrated marrows may represent direct tumoricidal T-cell
447 responses. Repeated waves of tumour growth and T-cell control over time may give rise to
448 memory skewing (Extended Data Fig. 9), akin to successive infections giving rise to terminal
449 memory cells through aging[12]. This could explain the lack of exhausted T-cells in myeloma,
450 as T-cell stimulation would be intermittent (dependent on tumour growth) versus chronic,
451 suggesting factors besides T-cell-intrinsic loss of functionality drives progression. However,
452 alternative processes may drive T-cell differentiation in myeloma: inflammation, pervasive in
453 the myeloma marrow[52], can drive non-canonical memory T-cell differentiation[53]. *In vitro*
454 validation of tumour-specific TCR clones and mapping their phenotype through disease
455 evolution will elucidate the role of T-cell specificity in myeloma.

456

457 As T-cell skewing tracked with disease advancement, it may identify donors at risk of early
458 progression. The ability to track this skewing in the PB makes it attractive for immune
459 prognostication (Fig. 3e). However, T-cell skewing was similar in asymptomatic SMM and
460 overt MM (Fig. 3). While this suggests functional anti-tumour responses occur in high-risk
461 precursor conditions, arguing for early intervention with T-cell-dependent immunotherapeutic
462 interventions such as T-cell engager therapy[45], it may preclude the use of T-cell skewing to
463 identify SMM patients at imminent risk of progression. Additionally, T-cell skewing was more
464 closely associated with serum paraprotein than clinical diagnosis (Extended Data Fig.7g).
465 This may have the potential to enhance existing paraprotein-based prognostication
466 particularly in the rare subset of patients with non-secretory disease[54]. Further work is needed
467 to explain the T-cell skewing-paraprotein association, but we note in addition to paraprotein
468 being an indicator of tumour bulk (thus, total tumour antigen burden or tumour-associated
469 inflammation) that malignant immunoglobulin-derived peptides can serve as immunogenic T-
470 cell epitopes[7,55]. The additional associations we identify between effector T-cells with marrow
471 infiltration and putative tumour-specificity with tumour antigen presentation-associated gene
472 expression may provide additional combinatorial opportunities for integrating immune and
473 clinical metrics into predictive measures of disease risk.
474
475 While we were unable to compare T-cells features and tumour genomic classification in our
476 dataset, T-cell skewing was previously shown to be enhanced in hyperdiploid patients[46].
477 Additionally, further work is needing to directly connect beneficial survival outcomes
478 associated with tumour MHC and stress (possibly death-related) gene expression (Fig. 5h,
479 Extended Data Fig. 2i) with T-cell differentiation and function. Finally, to understand how
480 tumour genomics relates to T-cell differentiation, it will also be important to longitudinally
481 profile neoantigen-reactive responses alongside tumour evolution.
482

483 Our results provide a conceptual framework for how T-cells are altered during myeloma
484 disease evolution and highlight the importance of contextualising immune heterogeneity with
485 tumour biology when using immune biomarkers in myeloma.
486

487 **Acknowledgements**

488 This work was funded by CRUK, the Medical Research Council, and the UCL/UCLH
489 Biomedical Research Centre. We thank members of the CARDMON, COSMOS and RADAR
490 teams, particularly Sayeh Foroughi, Ambreen Rashid and Grant Vallance, and the UCLH
491 Haematology Cancer Trials Unit. We thank all patients who participated in these studies.
492 Work at the CRUK City of London Centre Single Cell Genomics Facility and Cancer Institute
493 Genomics Translational Technology Platform was supported by the Cancer Research UK
494 (CRUK) City of London Centre Award [C7893/A26233]. We thank the International Myeloma
495 Society (IMS) for funding the presentation of this manuscript in abstract form at the 2022 and
496 2023 IMS Annual Meetings. We thank the authors of the publications whose data was re-
497 analysed for this study for making their data freely available, particularly David B. Sykes,
498 Samuel S. McCachren, Madhav V. Dhodapkar, Romanos Sklavenitis-Pistofidis, Irene M.
499 Ghobrial, Ola Landgren, Gareth J. Morgan, Francesco Maura and Reyka Jayasinghe. We
500 thank the Multiple Myeloma Research Foundation (MMRF), the Perelman Family Foundation.

501 **Methods**

502

503 *Primary clinical samples*

504 Bone marrow aspirates from individuals with myeloma or precursor conditions were obtained
505 from patients included in one of four ongoing clinical trials: (1) Defining risk in smouldering
506 myeloma (SMM) for early detection of multiple myeloma (COSMOS), a multicentre,
507 observational UK study in smouldering myeloma (NCT05047107); (2) Risk-Adapted therapy
508 Directed According to Response (RADAR), a randomised phrase II/III trial in newly diagnosed
509 patients with multiple myeloma eligible for transplant (UK-MRA Myeloma XV)[56]; (3)
510 Carfilzomib/Cyclophosphamide/Dexamethasone with Maintenance Carfilzomib in Untreated
511 Transplant-eligible Patients with Symptomatic MM to Evaluate the Benefit of Upfront ASCT
512 (CARDAMON), a phase II trial[57]; (4) Biology of Myeloma, an observational study open to all
513 plasma cell disorder patients treated at University College London Hospitals (Research ethics
514 committee reference: 07/Q0502/17). Bone marrow aspirates from non-cancer controls were
515 collected as a by-product of routine elective orthopaedic surgery (hip or knee replacements)
516 via the UCL/ UCLH Biobank for Studying Health and Disease (Research ethics committee
517 reference: 20/YH/0088). All material was obtained after written informed consent in
518 accordance with the Declaration of Helsinki.

519 For scRNA-seq experiments, bone marrow aspirates were collected in
520 ethylenediamine-tetraacetic acid (EDTA) and processed within 24 hours of collection.
521 Mononuclear cells (MNCs) were isolated by Ficoll Paque density gradient centrifugation,
522 using SepMate tubes (StemCell Technologies). Freshly isolated BM MNCs were analysed for
523 tumour infiltration by flow cytometry (LSRFortessa, 4 laser 16 color). Cells were stained with
524 the fluorochrome-conjugated antibody CD138 (PE, clone MI15, BioLegend), CD38 (PE-CY7,
525 Clone HB7, biolegend), and a fixable viability dye (eFluor 780, eBioscience). Tumour cell
526 marrow infiltration was determined as the frequency of live BM MNCs cells co-expressing

527 CD38 and CD138 as determined via manual gating (FlowJo v10, BD Biosciences) (Extended
528 Data Fig. 1f).
529 For CyTOF experiments, MNCs were isolated by Ficoll Paque density gradient
530 centrifugation, using SepMate tubes (StemCell Technologies) and cryopreserved in 90% FBS
531 and 10% DMSO for long-term storage in liquid nitrogen.
532
533 *scRNA-seq and scTCRseq sample and library preparation*
534 For newly-generated "T cell–enriched/depleted" samples T-cells were enriched from freshly
535 isolated BM MNCs by magnetic separation using a Pan T-cell Isolation Kit and CD15
536 MicroBeads (Miltenyi Biotec). After sorting, the T-cell depleted and enriched compartments
537 were pelleted and resuspended in 0.04% BSA in PBS at 10^6 cells/mL and loaded onto the
538 Chromium Controller (10X Genomics). For newly-generated "CD8-enriched" samples T-cells
539 were enriched using the same protocol with the addition of CD4 MicroBeads (Miltenyi Biotec)
540 and only CD8-enriched samples were loaded. This generated a total of 47 libraries. All
541 samples were processed using the Chromium Next GEM Single Cell 5' Dual Index Kit (10X
542 Genomics, v2) following manufacturers protocol. T-cell and CD8-enriched samples were
543 additionally processes using the VDJ kit (10x Genomics). The libraries were sequenced by
544 Illumina NovoSeq 6000. Sequencing data was processed with CellRanger GEX and VDJ
545 (v6.0.0) using the GRCh38-2020-A and vdj_GRCh38_alts_ensembl-5.0.0 human reference
546 genomes, respectively. Across samples Cellranger GEX called a median of 6367 cells and
547 Cellranger VDJ a median proportion of 0.76 cells with product V J spanning TRA and TRB
548 pairs.
549
550 *Filtering, integration, clustering, and dimensionality reduction of scRNA-seq data*
551 scRNA-seq data were analysed and integrated using the python packages scanpy (1.8.2) and
552 scvi-tools (0.15.2)[58,59]. Gene-barcode matrices for all newly-generated and re-analysed

553 samples were assigned unique sample-specific barcodes, merged, and subset to high-
554 quality cells for integration (minimum unique genes > 200, minimum total counts > 500, total
555 percentage mitochondrial chromosome-encoding transcripts < 10%, total percentage
556 transcripts encoding haemoglobin genes *HBB*, *HBA1* and *HBA2* < 20%). Cells called as
557 doublets by the python package scrublet[60] (0.2.3) were removed. Samples with < 100 high-
558 quality cells were removed prior to integration.

559 For integration, we utilised single-cell variation inference (scvi)[59]. A subset of 7000
560 highly variable genes across batches was calculated on log(x+1) normalised gene expression
561 with the function scanpy.pp.highly_variable_genes(adata, batch_key="batch") to identify
562 genes with consistently high inter-cellular variation across different batches. Specific gene
563 groups which can vary between cells for technical (mitochondrial, representing cell stress) or
564 irrelevant biological (immunoglobin and TCR genes, representing lymphocyte clonality)
565 reasons were excluded from highly variable genes to prioritise clustering on phenotype-
566 defining genes. The un-normalised expression of these 7000 variable genes was prepared
567 for scvi using the function scvi.model.SCVI.setup_anndata() with sample batch as the batch
568 key and sample identifier and 10x chemistry as categorical covariate keys. A scvi model was
569 then initialised with the following non-default parameters: scvi.model.SCVI(n_latent=30,
570 n_layers=2, dropout_rate=0.2, gene_likelihood="nb"). These parameters (number of HVGs,
571 number of latent dimensions and hidden layers, dropout rate) were selected through a
572 parameter sweep focused on minimising batch influence on integrated latent representation
573 and retaining biological identify (data not shown). Minimisation of batch influence was
574 assessed by linear regression of latent dimensions against batch covariates as implemented
575 by scib (https://github.com/theislab/scib). The retention of biological identity was assessed
576 by analysing the separation of CD4+ and CD8+ T-cells (the median log ratio of *CD4*-
577 expressing and *CD8A*-expressing cells closest to zero across clusters). This model was
578 trained for a maximum of 400*(20,000*x) epochs where x was the number of input cells.

579 Integration was first performed on all cells then repeated for just T-cell clusters using 5000
580 highly variable genes and gene_likelihood="nb" but otherwise identical parameters.
581 The latent representation of the trained scvi model was used to create a
582 neighbourhood graph using scanpy.pp.neighbors(adata, n_neighbors=10) for subsequent
583 graph-based clustering using the leiden algorithm. The size of the local neighbourhood
584 (n_neighbors=10) and Leiden clustering resolutions were selected for optimum granularity of
585 biological clusters. Analysis of the latent representation was used as input for creation of a
586 uniform manifold approximation and projection (UMAP, scanpy default parameters) or
587 Minimum-Distortion Embedding using the Python package pymde[61] (0.1.15). For visualisation
588 of a large number of cells on either UMAP or MDE, the R package scattermore (1.0) was used
589 to created rasterized dot plots.
590
591 *Differential expression and pathway analysis of scRNA-seq data*
592 Differential expression between specified conditions was performed using the R package
593 scran (1.26.2) function pairwiseTTests() between specified contrasts with batch as the
594 blocking level for each cell to model for batch effects. Genes were identified as significantly
595 differentially expressed with a false discovery rate (FDR, Benjamini and Hochberg-adjusted
596 *P* value) of < 0.1. Pathway analysis of differentially expressed genes was performed using the
597 R package fgsea (1.24.0) with gene set enrichment analysis of gene sets from BIOCARTA,
598 KEGG and REACTOME databases accessed via the R package msigdbr (7.5.1; Supplemental
599 Table 2).
600
601 *Phenotyping gene expression clusters from scRNA-seq data*
602 Cluster markers genes were calculated using log-normalised expression of all genes in a
603 study-aware fashion using the findMarkers function from the R package scran specifying
604 test.type="wilcox" and batch as the blocking level for each cell. This restricts differential

605 expression comparisons within individual sources and pools the downstream result, meaning
606 no inter-batch comparisons were performed. Marker genes were combined with supervised
607 analysis of the expression of known RNA and protein markers to phenotype clusters. Clusters
608 characterised by expression of known stress-associated genes (for example, *JUN*, *FOS*)[62] or
609 by co-expression of marker genes for independent phenotypes (for example, T and B cells)
610 were removed. For T-cell cluster phenotyping, clusters lacking expression of *CD3D*, *CD3E*
611 and *CD3G* or both *CD4* and *CD8A* were removed. *De novo* label prediction tools were run
612 with default parameters: Azimuth (https://azimuth.hubmapconsortium.org/) and Celltypst
613 (https://www.celltypist.org/). Manually curated T-cell naïve and cytotoxicity gene signatures
614 were taken from Chu et al.[63]. Gene sets were applied to cells using the R package UCell
615 (2.2.0)[76].
616
617 *Differential abundance analysis of scRNA-seq data*
618 We normalised cell type abundance following a compositional data framework[64]. For each
619 sample, cluster counts were derived and zero values replaced by a Bayesian-multiplicative
620 replacement strategy which preserves the ratios between non-zero clusters, implemented
621 using the R package zCompositions (1.4.0-1) function cmultRepl()[65], generating zero-imputed
622 pseudo-counts. The centered log-ratio (CLR) transformation was then used to transform
623 pseudo-counts relative to the geometric mean of all clusters in a given sample, implemented
624 using the R package compositions (2.0-6) function clr(). The CLR transformation thus reports
625 cell type abundance relative to the per-sample average seeking to reduce the mutual
626 dependency of proportional data[66].
627 For samples from Stephenson et al.[16], the median age of each age range was used
628 (for example, for the 50-55 group 52.5 was used). Several donors in the dataset were sampled
629 longitudinally, including Oetjen et al.[67] and Liu et al.[15]. In these cases, only the first longitudinal
630 timepoint was analysed unless otherwise specified.

631 Normalised cluster abundances were used as input for a combination of intercept-
632 only and additive regression models exploring the relationship between cluster abundance
633 and different conditions (for example, patient group, or patient group and age) as described.
634 Selected comparisons were also performed using a mixed-effect model with an additional
635 random effect term (for sample, study of origin), implemented using the R package lmerTest
636 (3.1-3) function lmer().
637
638 *Unsupervised ordination of T cell composition and calculation of exaggerated T-cell aging*
639 Normalised T cell cluster abundance was used as input for PCA using the R function
640 prcomp. Exaggerated T cell aging was calculated by first constructing a linear model
641 examining the relationship between PC1 and age for non-cancer controls only. Next, the age
642 of cancer patients was used to predict PC1 values for each patient in this model. The
643 difference between predicted and real PC1 values (residuals) for each patient was interpreted
644 as the difference between the T cell skewing expected for each patient's versus their
645 observed T cell skewing, respectively. These residuals-derived values were termed
646 "exaggerated T cell aging". A patient was considered to have exaggerated T cell aging if their
647 values were greater than zero (or, skewing was greater than expected for their age).
648
649 *scTCRseq pre-processing, clonal expansion calculation, T cell subset identification and*
650 *clustering*
651 TCR paired alpha and beta clones (also termed clonotypes) were defined by CellRanger VDJ
652 (raw_clonotype_id, clonotype_id) by matching shared V and J gene and CDR3 sequences for
653 alpha and beta TCR chains were appended to single cells by matching barcode. For scTCR-
654 seq derived from published data, we used published clone identifiers. Clonal expansion was
655 calculated as the abundance cells labelled with each clone identified in each sample. CD8+
656 and CD4+ clones were identified by aggregating expression of *CD8A*, *CD8B* and *CD8B2* or

657 *CD4*, respectively, across all cells for each clone. Clone subset was defined as CD4 (N cells
658 CD4 detected ≥ N cells CD8 detected), CD8 (CD8 < CD4), or double negative (DN, CD4 and
659 CD8 both zero; Extended Data Fig. 6a). Repertoire clonality was calculated among each
660 specific subset of cells (such as all T cells or CD8+ memory cells) with a minimum of 100
661 cells using Simpson's diversity index[68]. Clusters of TCRs with similar sequence features were
662 identified within a single patient's alpha or beta chain repertoire using tcrdist3 (0.2.2)[36] using
663 default parameters. TCR clustering networks were constructed and visualised using the R
664 package igraph (1.4.2).
665
666 *Annotation of HLA-matched viral reactivity-annotated TCR clones*
667 HLA genotypes for 19 patients were derived using arcasHLA[69] ran on Cellranger output bam
668 files (possessorted_genome_bam). All 19 patients were newly-sequenced for this study and
669 therefore a combination of T cell-enriched/depleted and CD8-enriched (Extended Data
670 Fig.1a). arcasHLA was ran on every sample for each patient. HLA genotype for class I and
671 class II HLA was almost entirely identical across samples for an individual. In the rare cases
672 of two different samples possessing different HLA, both predicted genotypes were ignored.
673 Each donor's repertoire was then compared against the annotated TCR reactivity
674 database VDJdb, IEDB and CEDAR[37–39] subset to TCRs with annotated reactivity against an
675 epitope from a single human virus: cytomegalovirus (CMV), Epstein Bar virus (EBV), Influenza
676 A, or severe acute respiratory syndrome coronavirus 2 (SARS-CoV-2). TCRs annotated as
677 reactive against more than one human virus were also removed. The viral dataset set was
678 further subset to HLA-matched sequences for each patient's HLA genotype. A query TCR
679 clone was annotated as putatively viral-reactive if at least one alpha or one beta chain CDR3
680 sequence perfectly matched a CDR3 annotated against the same virus in the database, and
681 this clone's paired chain also perfected matched or possessed a highly similar CDR3
682 sequence to the same virus in the same HLA background. CDR3 similarity was performed as

683 described previously[70]. Briefly, each TCR chain's CDR3 amino acid sequence was
684 deconstructed into a series of overlapping triplets. Pairwise similarity between two CDR3 was
685 defined as the number of shared triplets normalized to the number of triplets per comparison.
686

687 *Identification of predicted neoantigen-reactive TCR clones*

688 Paired whole exome sequencing was performed for two samples as previously described[71].
689 Nonsynonymous mutations were selected and translated to peptides using a custom script
690 in R. We considered peptides of length 8, 9 or 10 amino acids which contained the altered
691 peptide as potential neoantigens. The immunoglobulin domain as excluded. Intronic
692 mutations or splice variants were not considered. Binding of these to the patient's HLA class
693 1 alleles was performed using NetMHCpan (4.1)[72]. Neoantigen binding was deemed
694 significant if the mutant peptide bound the HLA allele with an IC50 of less than 500nm and
695 the wild type had an IC50 of >500nm.

696 All cases where the peptide-HLA (pHLA) binding criteria were satisfied were
697 considered as potential binding partners for each TCR identified in the sample. TCR–pHLA
698 binding was predicted using TEINet with the authors pretrained models and default settings
699 [73]. The highest scoring pHLA-TCR was considered the most likely binding partner. Among all
700 pHLA–TCR pairs, the phenotype of TCR clones with the highest prediction scores (>0.7) was
701 analysis.
702

703 *Identification of malignant plasma cell clones in scRNA-seq*

704 Patient plasma cells were isolated from the clustering of all cells (Fig.1) and patients with <
705 50 plasma cells were removed. This generated 67,656 plasma cells from 46 patients with a
706 median of 467 plasma cells each (range: 76–13,638). To identify tumour cells among plasma
707 cells, we leveraged the clonal plasma cell origin of myeloma. First, we attached the
708 expression of all available immunoglobin genes to each cell, after removing any gene filtered

709 performed earlier. Then, for each plasma cell, we identified the most highly expressed light
710 variable (kappa or lambda), heavy variable, and heavy constant chains. We next quantified
711 and ranked the abundance of every gene for each chain among an individual's plasma cells
712 (Extended Data Fig. 2a). Most individuals possessed a single gene for each chain which was
713 expressed by the majority of plasma cells (light variable median 95% range: 31-100%, heavy
714 constant median 96% range: 35-100%, heavy variable median 91% range: 24-100%). The
715 frequency of different light and heavy variable genes among tumour cells matched previously
716 reported frequencies in myeloma[74], including IGHV3-30 in 3 (6.5%) and IGKV1-39 in 2 (4.3%)
717 patients. We inferred that clonal immunoglobulin expression corresponded to clonal plasma
718 cells and labelled any plasma cell expressing the most highly abundant gene for each chain
719 in that donor as a tumour cell. This method yielded 67,048 predicted tumour cells. Predicted
720 tumour cells uniquely co-expressed clonal immunoglobulin genes (Extended Data Fig. 2b)
721 and expressed genes characteristic of their translocation subgroups (Extended Data Fig.
722 2c)[75], suggesting they did represent malignant cells.
723
724 *Transcriptional pathway analysis of tumour cells in scRNA-seq data*
725 To analysis tumour cell transcriptomes, we scored tumour cells by a set of pan-cancer
726 transcriptional pathways[25] using UCell. To compare the expression of individual pathways
727 between patients, we calculated the abundance of cancer cells highly expressing a given
728 pathway as the percentage of cells with expression greater than one standard deviation
729 above the median for each patient's tumour cells.
730
731 *De novo pathway enrichment in malignant cells*
732 To identify novel sets of genes enriched in malignant relative to normal plasma cells, we first
733 isolated each the tumour cells from each patient in turn. Next, we performed differential
734 expression between each patient's tumour cells only and all other plasma cells not classified

735 as malignant. Differential expression was only performed between cells from the same
736 sequencing batch. This yielded a set of malignant-enriched genes for each patient. Pathway
737 analysis was then performed as described. The pathways significantly enriched among
738 malignant-associated genes in four or more patients were identified (Extended Data Fig.8b).
739

740 *Transcriptional pathway survival analysis in CoMMpass*

741 We analysed an association of transcriptional pathways with overall survival in bulk RNA
742 sequencing samples from the CoMMpass cohort of newly-diagnosed MM patients[26], with
743 RNA sequencing data processed and normalised as described in Bauer et al.[77]. We calculated
744 the expression of each gene pathway by taking of each constituent gene in that pathway,
745 scaling expression between 0 and 1, and taking the average. We assessed the predictive
746 power of each pathway for overall and progression-free survival in patients using the
747 maximally selected rank statistic of the by R package maxstat (0.7-25), and analysed an
748 association between overall and progression-free survival and pathway expression above the
749 maxstat estimated cutpoint using a proportional hazards regression model using the R
750 package survival (3.5-5) with default parameters.
751

752 *CyTOF antibody staining, data acquisition and data pre-processing*

753 Details on antibodies are listed in Table S4. Conjugation of the purified antibodies with metal
754 reporters was performed with the MaxPar X8 and MaxPar MCP9 antibody labelling kits
755 (Fluidigm Sciences) according to the manufacturer's instructions. Frozen bone marrow MNCs
756 or the CD138-negative populations were thawed rapidly at 37°C and resuspended into pre
757 warmed thawing media of RPMI (Sigma-Aldrich) containing 20% FBS, 2mM EDTA
758 (pluriSelect) and 5mg DNase (Sigma-Aldrich). Cell suspensions were washes and filtered to
759 form a single cell suspension. Cells were incubated with 5μM Cell-ID Cisplatin (Fluidigm
760 Sciences) in serum free RPMI for 3 minutes at room temperature (rT) to identify dead cells.

761 Cells were then washes and incubated with human Fc block (BioLegend) for 10 minutes at
762 rT before being barcoded using a 6-choose-3 Cadmium CD45 Live Barcoding (Fluidigm
763 Sciences). All samples were stained in the same batch. After live cell barcoding, the combined
764 samples were then stained with metal-conjugated antibodies for surface antigens for 30
765 minutes at rT. After staining, cells were washed with MaxPar Cell Staining Buffer and
766 permeabilised with MaxPar nuclear antigen staining buffer before staining with metal-
767 conjugated antibodies for intracellular antigens. Cells were again washed and fixed using
768 1.6% paraformaldehyde. Cells were then incubated with Cell-ID intercalator-Ir (Fluidigm
769 Sciences) to stain all cells in MaxPar Fix and Perm Buffer (Fluidigm Sciences) and aliquoted
770 and frozen in cryovials. Stained samples were thawed and washed on the day of acquisition.
771 Cells were acquired on the Helios mass cytometer (Fluidigm Sciences). Data from
772 different days were normalized by using EQ Four Element Calibration Beads (Fluidigm
773 Sciences). Data was debarcoded using the Fluidigm CyTOF software and patient sample fcs
774 files run from different days were concatenated. Before downstream analysis, initial data
775 clean up was carried out using FlowJo. Live CD3+ cells were exported by manual gating on
776 Event_length, Residual, Offset, DNA (^{191}Ir and ^{193}Ir), live cells (^{195}Ir) and CD3 expression (^{89}Y).
777
778 *Downstream analysis of CyTOF data*
779 CyTOF data were analysed using a custom R pipeline modified from Nowicka et al.[78].
780 Protein expression data was normalised using the flowCore (2.10.0) logicleTransform()
781 function. Cells were clustered using T-cell markers (all unique proteins shown in Extended
782 Data Fig. 4) using FlowSOM (2.6.0) on a 12 x 12 node self-organising map. This generated
783 50 putative T-cell clusters. Only clusters expressing CD3 and either CD4 or CD8 were taken
784 retained. One cluster strongly co-expressing all markers was removed as a likely artifact. The
785 remaining clusters were merged to 17 final clusters based on homogeneous co-expression
786 of known T-cell marker genes (for example, CD8+CD45RA+CD45RO-IL7R+TCF7+ were

787 classified as naïve CD8+ T-cells). The expression of T-cell marker proteins for 1000 cells per-
788 sample was used to calculate a UMAP using the R package uwot (0.1.14) with the following
789 parameters umap(expression, n_neighbors=25, metric="cosine", spread=2, min_dist=0.1,
790 fast_sgd=TRUE) based on visual separation of clusters.
791
792 *Comparison of T-cell clusters across scRNA-seq and CyTOF*
793 First, T cell markers shared between the scRNA-seq and CyTOF datasets were identified.
794 These included (protein/RNA) TBET/*TBX21*, FOXP3/*FOXP3*, "TOX/*TOX*, LAG3/*LAG3*,
795 CTLA4/*CTLA4*, KLRG1/*KLRG1*, PD1/*PDCD1*, EOMES/*EOMES*, CD28/*CD28*, TCF1/*TCF7*,
796 CD69/*CD69*, CD4/*CD4*, CD8/*CD8A*, ICOS/*ICOS*, IL7R/*IL7R*, TIGIT/*TIGIT*, CD25/*IL2RA*,
797 KI67/*MKI67*, GZMB/*GZMB*, HLA-DR/*HLA-DRA*. We also restricted our analysis to scRNA-
798 seq clusters likely to be profiled using our existing CyTOF panel. Therefore, we removed the
799 interferon-expressing ISG.ISG15 and Teff.IFIT2 and invariant MAIT_gdT scRNA-seq clusters.
800 Additionally, we removed the proliferating T cell (Prolif.) scRNA-seq cluster, to avoid a
801 confusion when comparing to the CyTOF CD4.Tm-Prolif. and CD8.Tem-Prolif. clusters, which
802 were also removed. The average expression of each shared marker was scaled within
803 scRNA-seq or CyTOF clusters. The correlation between each cluster's shared markers was
804 calculated using Pearson correlation (Extended Data Fig.4d-e), with highly correlated clusters
805 inferred to represent the same underlying T cell phenotype.
806
807 *Statistical analyses*
808 For comparison of means in box plots, *P* values were calculated by two-sided Wilcoxon test
809 using the R package ggpubr (0.6.0). R and *P* values for correlations were calculated by
810 Pearson correlation. For hierarchal clustering on heatmaps, Euclidean distance was used as
811 the default distance measure.
812

Data availability

Published datasets were acquired following the instructions in each original publication. Specifically, data shared through the gene expression omnibus (GEO) can be accessed for Maura et al. under accession GSE161195, Bailur et al. under accession GSE163278, Oetjen et al. under accession GSE120221, Granja et al. under accession GSE139369, Zavidij et al. under accession GSE124310, Kfoury et al. under accession GSE143791, and Zheng et al. under accession GSE156728. Data shared via dbGaP for Sklavenitis-Pistofidis et al. can be accessed under accession phs002476.v1.p1. Data shared online can be accessed for Stephenson et al. (via https://covid19cellatlas.org/), Conde et al. (via https://www.tissueimmunecellatlas.org/), and Liu et al. (via https://explore.data.humancellatlas.org/projects/2ad191cd-bd7a-409b-9bd1-e72b5e4cce81). The integrated single-cell RNA and TCR datasets and cohort information are available online (https://zenodo.org/doi/10.5281/zenodo.11047959). CoMMpass data were downloaded from the MMRF researcher gateway (https://research.themmrf.org). Newly-generated raw sequencing data will be made publicly available and uploaded to the GEO upon peer-reviewed publication. Code to reproduce figures will be made available upon peer-reviewed publication or upon reasonable request.

831 **Supplemental tables**

832 Supplemental Table 1. Overview of donors included in single-cell RNA sequencing cohort.

833 Supplemental Table 2. Constituent genes for gene sets and pathways used throughout this

834 study.

835 Supplemental Table 3. Significantly differential expressed marker genes for T-cell clusters.

836 Supplemental Table 4. Information regarding CyTOF panel.

837 Supplemental Table 5. Differential expression results between clones with and without

838 putative viral-specificity annotations.

839

References

1. de Visser, K. E. & Joyce, J. A. The evolving tumor microenvironment: From cancer initiation to metastatic outgrowth. *Cancer Cell* **41**, 374–403 (2023).
2. Philip, M. & Schietinger, A. CD8+ T cell differentiation and dysfunction in cancer. *Nat. Rev. Immunol. 2021 224* **22**, 209–223 (2021).
3. Reading, J. L. *et al.* The function and dysfunction of memory CD8+ T cells in tumor immunity. *Immunological Reviews* vol. 283 194–212 (2018).
4. Kay Chung, H., McDonald, B. & Kaech, S. M. The architectural design of CD8+ T cell responses in acute and chronic infection: Parallel structures with divergent fates. *J. Exp. Med.* **218**, (2021).
5. Blank, C. U. *et al.* Defining 'T cell exhaustion'. *Nat. Rev. Immunol.* **19**, 665–674 (2019).
6. Chow, A., Perica, K., Klebanoff, C. A. & Wolchok, J. D. Clinical implications of T cell exhaustion for cancer immunotherapy. *Nat. Rev. Clin. Oncol. 2022 1912* **19**, 775–790 (2022).
7. van de Donk, N. W. C. J., Pawlyn, C. & Yong, K. L. Multiple myeloma. *The Lancet* vol. 397 410–427 (2021).
8. Bazarbachi, A. H., Al Hamed, R., Malard, F., Harousseau, J. L. & Mohty, M. Relapsed refractory multiple myeloma: a comprehensive overview. *Leukemia* **33**, 2343–2357 (2019).
9. Mateos, M. V. *et al.* International Myeloma Working Group risk stratification model for smoldering multiple myeloma (SMM). *Blood Cancer J. 2020 1010* **10**, 1–11 (2020).
10. Landgren, O. *et al.* Monoclonal gammopathy of undetermined significance (MGUS) consistently precedes multiple myeloma: A prospective study. *Blood* **113**, 5412–5417 (2009).
11. Ho, M. *et al.* Changing paradigms in diagnosis and treatment of monoclonal gammopathy of undetermined significance (MGUS) and smoldering multiple myeloma (SMM). *Leuk. 2020 3412* **34**, 3111–3125 (2020).
12. Mogilenko, D. A., Shchukina, I. & Artyomov, M. N. Immune ageing at single-cell resolution. *Nat. Rev. Immunol. 2021 228* **22**, 484–498 (2021).
13. Di Rosa, F. Maintenance of memory T cells in the bone marrow: survival or homeostatic proliferation? *Nat. Rev. Immunol. 2016 164* **16**, 271–271 (2016).
14. Bailur, J. K. *et al.* Early alterations in stem-like/marrow-resident T cells and innate and myeloid cells in preneoplastic gammopathy. *JCI Insight* **4**, (2019).
15. Liu, R. *et al.* Co-evolution of tumor and immune cells during progression of multiple myeloma. *Nat. Commun. 2021 121* **12**, 1–18 (2021).
16. Stephenson, E. *et al.* Single-cell multi-omics analysis of the immune response in COVID-19. *Nat. Med. 2021 275* **27**, 904–916 (2021).
17. Domínguez Conde, C. *et al.* Cross-tissue immune cell analysis reveals tissue-specific features in humans. *Science (80-.).* **376**, (2022).
18. Oetjen, K. A. *et al.* Human bone marrow assessment by single-cell RNA sequencing, mass cytometry, and flow cytometry. *JCI Insight* **3**, (2018).
19. Maura, F. *et al.* Genomic and immune signatures predict clinical outcome in newly diagnosed multiple myeloma treated with immunotherapy regimens. *Nat. Cancer 2023 412* **4**, 1660–1674 (2023).
20. Granja, J. M. *et al.* Single-cell multiomic analysis identifies regulatory programs in mixed-phenotype acute leukemia. *Nat. Biotechnol. 2019 3712* **37**, 1458–1465 (2019).
21. Zavidij, O. *et al.* Single-cell RNA sequencing reveals compromised immune microenvironment in precursor stages of multiple myeloma. *Nat. Cancer* **1**, 493–506 (2020).
22. Kfoury, Y. *et al.* Human prostate cancer bone metastases have an actionable immunosuppressive microenvironment. *Cancer Cell* **39**, 1464-1478.e8 (2021).
23. Sklavenitis-Pistofidis, R. *et al.* Immune biomarkers of response to immunotherapy in patients with high-risk smoldering myeloma. *Cancer Cell* **40**, 1358-1373.e8 (2022).
24. Zheng, L. *et al.* Pan-cancer single-cell landscape of tumor-infiltrating T cells. *Science (80-.).* **374**, (2021).
25. Gavish, A. *et al.* Hallmarks of transcriptional intratumour heterogeneity across a thousand tumours. *Nat. 2023*

887 *6187965* **618**, 598–606 (2023).
888 26. Skerget, S. *et al.* Genomic Basis of Multiple Myeloma Subtypes from the MMRF CoMMpass Study. *medRxiv*
889 2021.08.02.21261211 (2021) doi:10.1101/2021.08.02.21261211.
890 27. Nutt, S. L., Hodgkin, P. D., Tarlinton, D. M. & Corcoran, L. M. The generation of antibody-secreting plasma cells. *Nat.*
891 *Rev. Immunol.* **15**, 160–171 (2015).
892 28. Szabo, P. A. *et al.* Single-cell transcriptomics of human T cells reveals tissue and activation signatures in health and
893 disease. *Nat. Commun.* **10**, 1–16 (2019).
894 29. Ren, X. *et al.* Insights Gained from Single-Cell Analysis of Immune Cells in the Tumor Microenvironment.
895 *https://doi.org/10.1146/annurev-immunol-110519-071134* **39**, 583–609 (2021).
896 30. Cano-Gamez, E. *et al.* Single-cell transcriptomics identifies an effectorness gradient shaping the response of CD4+ T
897 cells to cytokines. *Nat. Commun. 2020 111* **11**, 1–15 (2020).
898 31. Kared, H., Martelli, S., Ng, T. P., Pender, S. L. F. & Larbi, A. CD57 in human natural killer cells and T-lymphocytes.
899 *Cancer Immunol. Immunother.* **65**, 441–452 (2016).
900 32. Omilusik, K. D. *et al.* Transcriptional repressor ZEB2 promotes terminal differentiation of CD8+ effector and memory
901 T cell populations during infection. *J. Exp. Med.* **212**, 2027–2039 (2015).
902 33. Khan, O. *et al.* TOX transcriptionally and epigenetically programs CD8+ T cell exhaustion. *Nat. 2019 5717764* **571**,
903 211–218 (2019).
904 34. Greipp, P. R. *et al.* International staging system for multiple myeloma. *J. Clin. Oncol.* **23**, 3412–3420 (2005).
905 35. Pauken, K. E. *et al.* TCR-sequencing in cancer and autoimmunity: barcodes and beyond. *Trends Immunol.* **43**, 180–
906 194 (2022).
907 36. Dash, P. *et al.* Quantifiable predictive features define epitope specific T cell receptor repertoires. *Nature* **547**, 89
908 (2017).
909 37. Bagaev, D. V. *et al.* VDJdb in 2019: database extension, new analysis infrastructure and a T-cell receptor motif
910 compendium. *Nucleic Acids Res.* **48**, D1057–D1062 (2020).
911 38. Fleri, W. *et al.* The immune epitope database and analysis resource in epitope discovery and synthetic vaccine
912 design. *Front. Immunol.* **8**, 250318 (2017).
913 39. Koşaloğlu-Yalçın, Z. *et al.* The Cancer Epitope Database and Analysis Resource (CEDAR). *Nucleic Acids Res.* **51**,
914 D845–D852 (2023).
915 40. Kourelis, T. V. *et al.* Mass cytometry dissects T cell heterogeneity in the immune tumor microenvironment of common
916 dysproteinemias at diagnosis and after first line therapies. *Blood Cancer J.* **9**, (2019).
917 41. Meermeier, E. W., Bergsagel, P. L. & Chesi, M. Next-Generation Therapies for Multiple Myeloma. *Annu. Rev. Cancer*
918 *Biol.* **8**, (2024).
919 42. Galletti, G. *et al.* Two subsets of stem-like CD8+ memory T cell progenitors with distinct fate commitments in
920 humans. *Nat. Immunol. 2020 2112* **21**, 1552–1562 (2020).
921 43. Mogilenko, D. A. *et al.* Comprehensive Profiling of an Aging Immune System Reveals Clonal GZMK+ CD8+ T Cells as
922 Conserved Hallmark of Inflammaging. *Immunity* **54**, 99-115.e12 (2021).
923 44. Hudson, W. H. & Wieland, A. Technology meets TILs: Deciphering T cell function in the -omics era. *Cancer Cell* **41**,
924 41–57 (2023).
925 45. Friedrich, M. J. *et al.* The pre-existing T cell landscape determines the response to bispecific T cell engagers in
926 multiple myeloma patients. *Cancer Cell* (2023) doi:10.1016/J.CCELL.2023.02.008.
927 46. Dang, M. *et al.* Single cell clonotypic and transcriptional evolution of multiple myeloma precursor disease. *Cancer*
928 *Cell* **41**, 1032-1047.e4 (2023).
929 47. Ludwig, H., Meckl, A. & Engelhardt, M. Compliance with vaccination recommendations among patients with multiple
930 myeloma: A real world experience. *HemaSphere* (2021) doi:10.1097/HS9.0000000000000597.
931 48. Lian, J., Yue, Y., Yu, W. & Zhang, Y. Immunosenescence: a key player in cancer development. *J. Hematol. Oncol.*
932 *2020 131* **13**, 1–18 (2020).
933 49. Noonan, K. *et al.* Activated marrow-infiltrating lymphocytes effectively target plasma cells and their clonogenic
934 precursors. *Cancer Res.* **65**, 2026–2034 (2005).

50. Spisek, R. *et al.* Frequent and specific immunity to the embryonal stem cell–associated antigen SOX2 in patients with monoclonal gammopathy. *J. Exp. Med.* **204**, 831 (2007).
51. Vuckovic, S. *et al.* Inverse relationship between oligoclonal expanded CD69- TTE and CD69+ TTE cells in bone marrow of multiple myeloma patients. *Blood Adv.* **4**, 4593–4604 (2020).
52. de Jong, M. M. E. *et al.* The multiple myeloma microenvironment is defined by an inflammatory stromal cell landscape. *Nat. Immunol. 2021 226* **22**, 769–780 (2021).
53. Henson, S. M. & Akbar, A. N. Memory T-cell homeostasis and senescence during aging. *Adv. Exp. Med. Biol.* **684**, 189–197 (2010).
54. Zamir, I. *et al.* Multiple Myeloma Oligosecretory Relapse, a Non-Negligible Phenomenon. Frequency, Clinical Characteristics and Outcomes in a Single Center. *Blood* **138**, 3772–3772 (2021).
55. Trojan, A. *et al.* Immunoglobulin framework-derived peptides function as cytotoxic T-cell epitopes commonly expressed in B-cell malignancies. *Nat. Med. 2000 66* **6**, 667–672 (2000).
56. Royle, K. L. *et al.* Risk and response adapted therapy following autologous stem cell transplant in patients with newly diagnosed multiple myeloma (RADAR (UK-MRA Myeloma XV Trial): study protocol for a phase II/III randomised controlled trial. *BMJ Open* **12**, (2022).
57. Yong, K. *et al.* Upfront autologous haematopoietic stem-cell transplantation versus carfilzomib-cyclophosphamide-dexamethasone consolidation with carfilzomib maintenance in patients with newly diagnosed multiple myeloma in England and Wales (CARDAMON): a randomised, phase 2, non-inferiority trial. *Lancet. Haematol.* **10**, e93–e106 (2023).
58. Wolf, F. A., Angerer, P. & Theis, F. J. SCANPY: Large-scale single-cell gene expression data analysis. *Genome Biol.* **19**, 1–5 (2018).
59. Gayoso, A. *et al.* A Python library for probabilistic analysis of single-cell omics data. *Nat. Biotechnol. 2022 402* **40**, 163–166 (2022).
60. Wolock, S. L., Lopez, R. & Klein, A. M. Scrublet: Computational Identification of Cell Doublets in Single-Cell Transcriptomic Data. *Cell Syst.* **8**, 281-291.e9 (2019).
61. Agrawal, A., Ali, A. & Boyd, S. Minimum-Distortion Embedding. *Found. Trends Mach. Learn.* **14**, 211–378 (2021).
62. Araúzo-Bravo, M. J., Izeta, A. & Ascensión, A. M. The need to reassess single-cell RNA sequencing datasets: the importance of biological sample processing. *F1000Research* **10**, (2021).
63. Chu, Y. *et al.* Pan-cancer T cell atlas links a cellular stress response state to immunotherapy resistance. *Nat. Med. 2023 296* **29**, 1550–1562 (2023).
64. Quinn, T. P. *et al.* A field guide for the compositional analysis of any-omics data. *Gigascience* **8**, 1–14 (2019).
65. Palarea-Albaladejo, J. & Martín-Fernández, J. A. zCompositions — R package for multivariate imputation of left-censored data under a compositional approach. *Chemom. Intell. Lab. Syst.* **143**, 85–96 (2015).
66. Aitchison, J. The Statistical Analysis of Compositional Data. *J. R. Stat. Soc. Ser. B* **44**, 139–160 (1982).
67. Oetjen, K. A. *et al.* Human bone marrow assessment by single-cell RNA sequencing, mass cytometry, and flow cytometry. *JCI insight* **3**, (2018).
68. Simpson, E. H. Measurement of diversity [16]. *Nature* **163**, 688 (1949).
69. Orenbuch, R. *et al.* arcasHLA: high-resolution HLA typing from RNAseq. *Bioinformatics* **36**, 33–40 (2020).
70. Joshi, K. *et al.* Spatial heterogeneity of the T cell receptor repertoire reflects the mutational landscape in lung cancer. *Nat. Med. 2019 2510* **25**, 1549–1559 (2019).
71. Walker, I. G. *et al.* Machine learning from the CARDAMON trial identifies a carfilzomib-specific mutational response signature. *medRxiv* 2023.04.08.23288287 (2023) doi:10.1101/2023.04.08.23288287.
72. Reynisson, B., Alvarez, B., Paul, S., Peters, B. & Nielsen, M. NetMHCpan-4.1 and NetMHCIIpan-4.0: improved predictions of MHC antigen presentation by concurrent motif deconvolution and integration of MS MHC eluted ligand data. *Nucleic Acids Res.* **48**, W449–W454 (2020).
73. Jiang, Y., Huo, M. & Li, S. C. TEINet: a deep learning framework for prediction of TCR–epitope binding specificity. *Brief. Bioinform.* **24**, 1–10 (2023).
74. González, D. *et al.* Immunoglobulin gene rearrangements and the pathogenesis of multiple myeloma. *Blood* **110**,

3112–3121 (2007).

75. Kaiser, M. F. *et al.* A TC classification-based predictor for multiple myeloma using multiplexed real-time quantitative PCR. *Leuk. 2013 278* **27**, 1754–1757 (2013).

76. Andreatta, M. & Carmona, S. J. UCell: Robust and scalable single-cell gene signature scoring. *Comput. Struct. Biotechnol. J.* **19**, 3796–3798 (2021).

77. Rasche, L. *et al.* Spatial genomic heterogeneity in multiple myeloma revealed by multi-region sequencing. *Nat. Commun.* **8**, (2017).

78. Nowicka, M. *et al.* CyTOF workflow: differential discovery in high-throughput high-dimensional cytometry datasets. *F1000Research 2019 6748* **6**, 748 (2019).